



Facultad de Ciencias

**SIMULATIONS FROM SECOND PRINCIPLES OF
SrTiO₃ POLARONS**

(Simulaciones desde segundos principios de polarones en SrTiO₃)

Trabajo de Fin de Máster
para acceder al título de

**MÁSTER INTERUNIVERSITARIO EN QUÍMICA
TEÓRICA Y MODELIZACIÓN COMPUTACIONAL**

Autor: Nayara Carral Sainz

Director: Javier Junquera Quintana

Julio-2021

ACKNOWLEDGEMENTS

En primer lugar, me gustaría mencionar a mi director del trabajo, Javier Junquera. Quiero darle las gracias por su permanente dedicación, por su paciencia a la hora de resolver cualquier tipo de duda y toda la motivación ha generado en mí en el desarrollo de este trabajo de fin de Máster, que espero que sea la primera semilla de una interesante y apasionante investigación.

Por otra parte, también me gustaría darle las gracias al profesor Pablo García. Con la mejor actitud, ha respondido a las innumerables dudas que me he planteado, en especial sobre MODELMAKER. También, darle las gracias por su apoyo en esta carrera de fondo.

Me gustaría agradecer también el apoyo de toda mi familia, en especial de mi madre y de mi hermana, mi mayor cómplice. Por su preocupación, por su curiosidad en lo que hago y por su confianza en todas las decisiones que he tomado en lo académico además de lo personal.

Por último quiero darle las gracias a mis amigos, en particular a mi amiga Carmen y Raquel, y a mis compañeros de la universidad por todas las conversaciones de desahogo y sobre todo, por los buenos momentos.

ABSTRACT

In the present work we have parametrized, for the first time, a tight binding model. The parametrization has been performed in order to carry out simulations of SrTiO₃ system employing larger size scales and reducing computational cost with regard to first principles calculations. The model is generated employing a python script called MODELMAKER. This toolbox links first-principles simulations obtained from the SIESTA code for a training set of configurations with the associated second-principles simulations, performed with SCALE-UP. Furthermore, both electron-electron interaction and electron-lattice coupling are included in the parameterization of the model. Thus, the obtained model is able to reproduce the band structure of SrTiO₃ configurations where the system has not been trained, such as a ferroelectric or antiferrodistortive phases.

This study opens the door to the performance of simulations in SrTiO₃ with thousands of atoms and capable of hosting polarons (localized electron in an octahedron of TiO₄ due to its associated cloud of phonons). Based on this polaronic model, the negative capacitance observed at the interface between SrTiO₃ and LaAlO₃ can be explained.

KEYWORDS

SrTiO₃, tight binding parametrization, negative capacitance, polaron, first-principles calculations, second-principles calculations

RESUMEN

En el presente trabajo se ha parametrizado por primera vez un modelo de enlace fuerte para la simulación del SrTiO₃ en escalas de tiempo y tamaño superiores a las que se pueden realizar desde primeros principios. El modelo es generado por medio del fichero de python llamado MODELMAKER, que enlaza las simulaciones de primeros principios de una colección de sistemas de entrenamiento utilizando el programa SIESTA, con las resultantes de segundos principios, efectuadas con SCALE-UP. Además, en la parametrización del modelo, se incluye tanto la interacción electrón-electrón como la dependencia con las interacciones electrón-red. Así, el modelo obtenido es capaz de reproducir la estructura de bandas de configuraciones de SrTiO₃ donde el sistema no ha sido entrenado, como una fase ferroeléctrica o un sistema antiferrodistortivo.

De esta forma, este estudio nos abre la puerta para la realización de simulaciones en SrTiO₃ con miles de átomos capaces de albergar polarones (electrón localizado en un octaedro de TiO₄ debido a la nube de fonones que lo acompañan). En base a este modelo polarónico puede explicarse la capacidad negativa observada en la interfase entre SrTiO₃ y LaAlO₃.

PALABRAS CLAVE

SrTiO₃, parametrización de enlace fuerte, capacidad negativa, polarón, cálculos de primeros-principios, cálculos de segundos-principios

Contents

1	Polar catastrophe	3
2	Negative compressibility	5
2.1	Mannhart's experiment	7
2.2	Critical analysis	8
2.3	Our proposal	9
2.4	Challenges	10
3	Electronic structure SrTiO₃	11
3.1	SrTiO₃ band diagram and projected density of states	11
3.2	Wannier functions	12
4	Computational Methods	15
4.1	Band diagram from First principles calculations	15
4.2	Tight binding in Wannier functions	16
4.3	Parametric one-electron Hamiltonian	18
4.4	Calculation of the model parameters	29
4.5	Steps in the model generation	31
5	Results	37
5.1	Ferroelectric phase in SrTiO ₃	37
5.2	Antiferrodistortive phase in SrTiO ₃	38
6	Conclusions	40
	Bibliography	41

Introduction

The concept behind this work is that a deeper quantitative understanding and engineering of quantum electronic properties at interfaces between oxide compounds in artificial layered systems will lead major technological advances. The unique properties emerging at these interfaces would allow us to address technological problems at the forefront of fundamental and applied research, including the realization of gate capacitors in metal-oxide-semiconductors field-effect transistors with unprecedented capacitance, or new thermoelectric, superconducting, or magnetoelectric devices.

Besides the fascination of complex oxides at the bulk level, when two of them are brought together, a host of phenomena can occur at their interface, the structural quality of which now rivals that of the best conventional semiconductors. Interfaces are rarely passive boundaries between the two materials. At the interface different properties couple, different phases compete, and sometimes totally new and unexpected phenomena emerge [28]. An extraordinary example is the appearance of a two-dimensional electron gas (2-DEG) with very high mobility and densities difficult to achieve in conventional semiconductors at the interface between two insulating oxides such as SrTiO₃/LaAlO₃ [22].

Despite the recent advances, the field of oxide interfaces remains largely unexplored. At this point theoretical guidance might be of great help. Improvements in the field of first and second-principles calculations, combined with the recurrent increase of computational power, allow not only accurate reproduction of experimental measurements but also trustable predictions. There is thus a strong motivation to further investigate oxide interfaces for predicting and engineering their properties.

In this work we shall exploit the property of the negative compressibility of diluted two-dimensional electron gases, in particular, in the SrTiO₃/LaAlO₃ interface. This quantum phenomenon offers an alternative mechanism for the enhancement of the capacitance. Several approaches have been suggested to explain the origin of the negative capacitance at these interfaces. However, since they are firmly rooted on the physics of semiconductors, they present problems when applied to 2-DEG generated at oxide interfaces. Within this work we propose an innovative mechanism to explain the unconventional phenomenon of negative electron compressibility. We establish that the electrons would be localized in polarons within the SrTiO₃ layer.

The theoretical simulation of the processes involved in this model poses a major problem that cannot be tackled with current state-of-the-art methodologies. Here we develop new atomistic simulation tools to access larger time and length scales than in conventional DFT, able to capture the relevant physics of the devices under working conditions. In particular, this work will be focused on the description of the MODELMAKER toolbox. This software is based on second principles calculations and is able to parametrized the terms of the hamiltonian employing first principles calculations.

The work is presented according to the following structure. Firstly, Chapter 1 explains the surprising conductivity of the interface between the insulators LaAlO₃ and SrTiO₃ by the *polar catastrophe model*. In Chapter 2 the concept of negative compressibility is exposed and the experimental evidence of this phenomenon is specifically mentioning by Mannhart experiments. Moreover, here we present our proposal, based on the explanation of the negative capacitance by the formation of polarons in SrTiO₃. The challenges of simulating these pseudoparticles are exposed at the end of

the chapter. The electronic structure of SrTiO₃ is studied in Chapter 3. Chapter 4 exhibits the developed computational method, based on second principle calculations. The results of the work are shown in Chapter 5. Finally, the conclusions are summarized in Chapter 6.

POLAR CATASTROPHE

Polar catastrophe was a pioneering model developed to explain the formation of quasi-two dimensional electron gas (2DEG) in SrTiO₃/LaAlO₃[001] interface [9]. The bedrock of this model is the layer charges imbalance between LaAlO₃ and SrTiO₃ planes oriented along the [001] direction. The polar catastrophe phenomenon is reasoned in respect of the electrostatics of the formal charges on each layer, which are computed by the oxidation number on each ion. The stacking of [001] atomic layers in a ABO₃ perovskite ($A \in \{\text{Sr}, \text{La}\}$ and $B \in \{\text{Ti}, \text{Al}\}$ for SrTiO₃ and LaAlO₃ respectively) is AO/BO₂/AO/BO₂. Thus, LaAlO₃[001] is composed by a sequence of positive charged (Al³⁺O₂⁻²)⁺¹ and negative charged (La⁺³O⁻²)⁻¹ planes. Whereas, SrTiO₃[001] combines two neutral layers, (Ti⁺⁴O₂⁻²)⁰ and (Sr⁺²O⁻²)⁰. A polar discontinuity is generated between the polar LaAlO₃ material and the nonpolar SrTiO₃ planes.

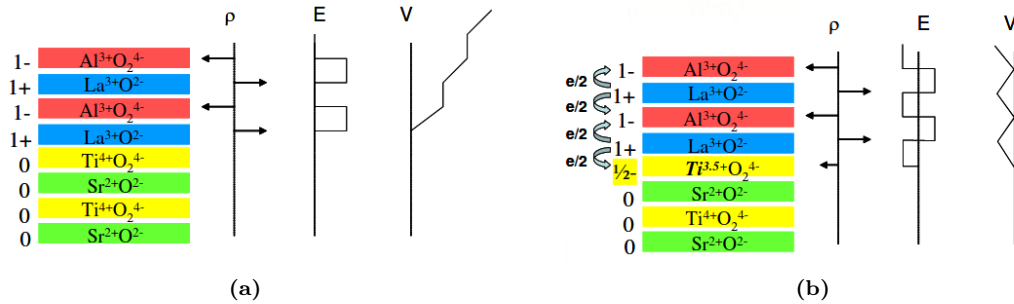


Figure 1.1. Schematic representation of polar catastrophe model for STO/LAO[001] interface. (a) In the absence of charge transfer, SrTiO₃ layers are neutral while the LaAlO₃ planes have alternating net charge (ρ). As result, a non-negative electric field arises in LaAlO₃ side causing a diverging electric potential V . This potential rises with the increase of LaAlO₃ thickness. (b) Once the transference has been produced, the average electric field in null and the electric potential finite [21].

Dealing with a well oxidized materials and focusing in a SrTiO₃/LaAlO₃ system with an n -type interface ((LaO)⁺/(TiO₂)⁰ contacting terminated layers), from the polar discontinuity an electric field \mathcal{E}_{LAO} arises in the polar material. Due to this electric field, a non-zero potential V_{LAO} appears in LaAlO₃ film which increases proportionally to its thickness, as shown in Fig. 1.1(a), tilting its respective electronic bands. Once the potential in LaAlO₃ has risen a critical value, the bottom conduction band in LaAlO₃ reaches the top of the SrTiO₃ conduction band. As consequence, a Zenner breakdown is produced, a charge transfer from BV_{LAO} to BC_{STO} is originated and the carriers from LaAlO₃ surface accumulates on the SrTiO₃ side of the interface. Each LaAlO₃ unit cell donates a electronic charge of $e/2$ (where e is negative). The electronic charge is transferred to the bottom of the conduction band of SrTiO₃. As we shall see in Chapter 3, the states located in this position are t_{2g} states, associated to $3d$ -orbitals $\{d_{xy}, d_{yz}, d_{xz}\}$. Then, the Ti ions placed in the interface become Ti^{+3.5}. This extra 1/2 electron can be measured by transport or spectroscopic techniques. Once the transference has been performed, an interface dipole is generated which causes oscillations of the electric field around 0 (electric field null in average). Then, the potential remains finite [21]. This process is displayed in Fig. 1.1(b).

As stated above, the formation of the 2DEG depends on V_{LAO} . If the potential doesn't reach the critical value, the valence and band conduction don't overlap and the interface keeps insulating. This critical electric potential is linked to the LaAlO_3 thickness, specifically conducting phenomenon in the interface is observed when the LaAlO_3 layers exceed the four unit cells according to Thiel and coworkers studies [6].

Finally, in addition to n -type interfaces, $\text{SrTiO}_3/\text{LaAlO}_3[001]$ interface can be composed by AlO_2/SrO exhibiting a p -type system. This one is insulating independently of LaAlO_3 thickness.

Considering insulating and paramagnetic systems, fascinating phenomena appear in polar oxide interfaces as the generation of a metallic state, ferromagnetism or even superconductivity. In addition to these properties, Mannhart [15] showed in their experiments the presence of negative compressibility.

NEGATIVE COMPRESSIBILITY

The unceasing research of high-speed, smaller and more efficient energetically micro-electronic devices points to Moore’s law, which states that the number of transistors that can be placed on an integrated circuit doubles approximately every two years. Currently, the typical transistor employed in the fabrication of electronic equipment is the the metal-oxide-semiconductor field-effect transistor (MOSFET). In a MOSFETs the principal component is a capacitor composed by the stack of three materials: a gate metal electrode, a semiconducting channel (which connects drain and source terminals) and an insulating oxide separating the previous elements. A voltage applied to the gate controls the resistance of the channel amplifying or switching electronic signals (the resistance of the channel is determined by “free charge” which is stored on the semiconductor). Thus, the capacitor is in charge of increasing the channel conductivity and efficiency operating the transistor at low gate voltages. As consequence, a large capacitance C is mandatory.

A capacitor is modeled by two parallel plates with a capacitance C_{geom} ,

$$C_{\text{geom}} = \frac{\epsilon_0 \epsilon A}{d}, \quad (2.1)$$

where ϵ_0 is the permittivity of vacuum, A is the lateral capacitance area, and ϵ and d are, respectively, the relative dielectric constant and the thickness of the dielectric [11]. The requirement of more powerful devices demands a reduction of capacitor area A to pack in a chip a larger number of transistors [3]. The problem now is focused on: how to reduce the area A maintaining the capacitance C as high as possible?

Traditionally, the established strategies have pursued the reduction of the gate dielectric thickness, d . The employed dielectric, archetypically silica (SiO_2), has been narrowed in the evolution of the electronic mechanisms until reaching the limit of around 1 nm. Below a critical dielectric thickness, this reduction cannot be sustained any longer due to the appearance of leakage electric currents producing tunneling effects between the capacitor’s plates, which increases the power consumption and overheats transistors. The use of a dielectric with larger ϵ [26] entailed an alternative solution. The chosen material was hafnia-based dielectrics. However, this material presented high oxygen diffusivities that compromise interface quality.

In 2009 a ground breaking work by Kopp and Mannhart [13] introduced an impressively proposal of capacitance enhancement. An alternative mechanism to rise the capacitance is needed, i.e., how we increase the capacitance beyond C_{geom} ? Up to now, the capacitor has been hypothesized as classical. As result, the electronic charge density in the capacitor is assumed to be of zero thickness and the density of states (DOS) is considered infinite, namely, including an extra electron doesn’t produce an energy cost.

An unprecedented proposal for capacitance enhancement is contemplated. This novel paradigm establishes the capacitance considering the quantum nature of the electrodes, moving beyond geometrical factors. Quantum and geometrical contributions can be examined independently resulting two capacitors connected in series.

Hereunder, the equivalent capacitance of several capacitors connected in series is evaluated. Se-

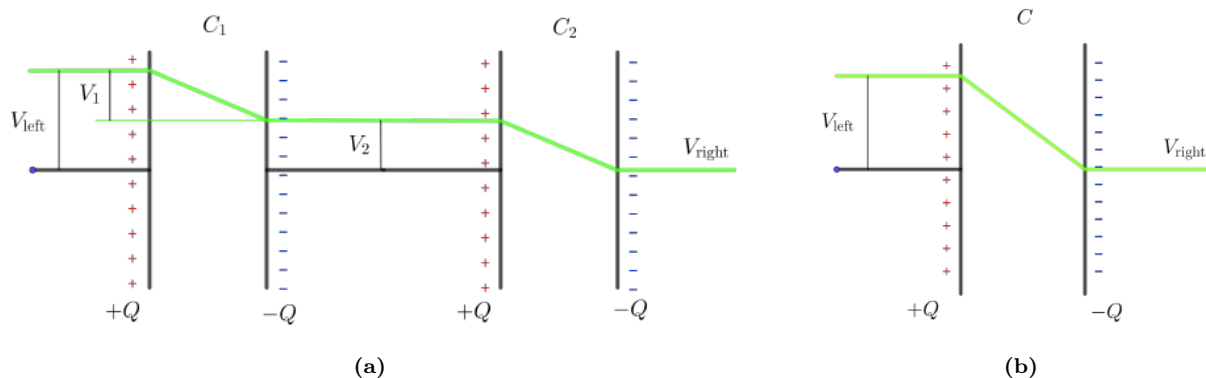


Figure 2.1. (a) Representation of two parallel-plate capacitors connected in series. The net charge contained in the plates is equal and with opposite signs at each capacitor. (b) Equivalent capacitor. Potential is shown by a green line. The drop is higher in the equivalent capacitor than either of the other two capacitors. Reproduced with permission from [20].

lecting two capacitors, whose capacitances are C_1 and C_2 respectively, the equivalent capacitance C is computed as

$$C = \left(\frac{1}{C_1} + \frac{1}{C_2} \right)^{-1}. \quad (2.2)$$

Figure 2.1(a) shows the electrostatic potential of two capacitors connected in series and characterized by $+Q$ and $-Q$ charges in the electrodes. Each plate has the same amount of net charge, with opposite signs at each capacitor. The equivalent capacitor is depicted in Fig. 2.1(b). According to the previous expression, elementary electrostatics establishes that the equivalent capacitance of several capacitors in series is always lower than the capacitance of the individual capacitors,

$$C < \min\{C_1, C_2\}. \quad (2.3)$$

Nevertheless, if some of the individual capacitances contributes negatively as shown in Fig. 2.2, the equivalent capacitance may be larger than each one of the components due to a reduction of the voltage difference. As consequence, the capacitance is enhanced beyond the expected classically, $C > C_{\text{geom}}$.

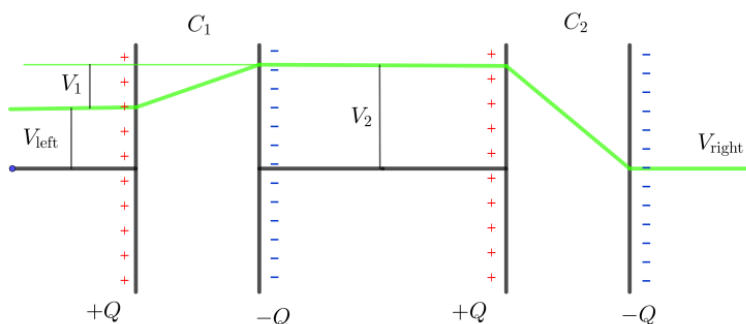


Figure 2.2. Representation of two parallel-plate capacitors connected in series. Left capacitor is characterized by a negative capacitance, $C_1 < 0$, while the right one capacitance is positive $C_2 > 0$. The presence of the negative capacitor causes an amplification in the potential than the two positive capacitances case. Reproduced with permission from [20].

A priori, it seems impossible to have a capacitor with negative capacitance. From a thermodynamical point of view, a capacitor with total negative capacitance is unstable. To provide better insight into this statement, the relationship between the capacitance and the energy of a system is shown

below,

$$C^{-1} = \left. \frac{d^2 E_{tot}}{dQ^2} \right|_{Q=0}. \quad (2.4)$$

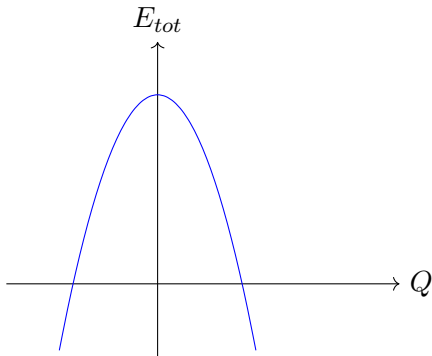


Figure 2.3. A system with a total negative capacitance (curvature) exhibits an unstable equilibrium. The addition of charge decreases the energy.

Regarding Eq.(2.4), a capacitor with negative capacitance will display a dependence of the total energy with respect to the charge as the one shown in Fig. 2.3. If the capacitance is negative, the addition of charge indefinitely reduces the energy. Therefore, it is clear that a capacitor with total negative capacitance is not stable. But this doesn't preclude that a part of the capacitor works with a local negative capacitance. According to Eq. (2.2), the total capacitance could be positive but larger than any of the individual capacitances connected in series. But which part of the capacitor may act as such as negative capacitance? In their pioneer work, Kopp and Mannhart [13] suggested that this is possible considering the quantum nature of the electrodes. Indeed they showed how the inverse of the quantum capacitance, C_q , is related with the electronic compressibility $\kappa = n^{-2}(dn/d\mu)$.

$$\frac{1}{C_q} = \frac{1}{Ae^2} \cdot \frac{d\mu}{dn}, \quad (2.5)$$

where μ represents the chemical potential and n the electron density.

The proposed model is based on the following characteristics.

- They assumed an ideal two-dimensional electron-gas (2DEG).
- The electrons were confined in a perfect two-dimensional plane of zero thickness, where the charge density is homogeneous.
- The total energy (E_{tot}) of the system was approximated considering the two more relevant contributions: exchange (E_X) [15] and kinetic (E_K) energies,

$$E_{tot} = E_K + E_X, \quad (2.6)$$

where

$$E_K = \frac{\hbar^2 \pi}{2m^*} n^2 \quad E_X = -\frac{1}{3} \sqrt{\frac{2}{\pi}} \frac{e^2}{\pi \epsilon} n^{\frac{3}{2}}. \quad (2.7)$$

The authors attributed the origin of negative compressibility to the prevalence in the low-density regime of exchange quantum energy, E_X , in electron-electron interactions on kinetic effects. This reasoning is justified by the calculation of $d\mu/dn$ employing Eq. (2.6),

$$\frac{d\mu}{dn} = \frac{d^2 E_{tot}}{dn^2} = \frac{\hbar^2 \pi}{m^*} - \sqrt{\frac{2}{\pi}} \frac{e^2}{4\pi \epsilon} n^{-\frac{1}{2}}, \quad (2.8)$$

where decreasing the electron density leads to negative infinity exchange energy. In this expression, m^* is the effective mass of the mobile electrons.

2.1 MANNHART'S EXPERIMENT

Experimental results based on previous model were performed by Mannhart and coworkers two years later [14]. The study was focused on the two-dimensional electron gas formed in $\text{SrTiO}_3/\text{LaAlO}_3$

interface diluted by the application of a gate voltage V_g in three different capacitor devices. Varying this potential, the capacitance, C , was measured for different frequencies. According to the observed results in Fig. 2.4(a) (measurements obtained for a capacitor made of a LaAlO_3 film deposited onto the top of SrTiO_3 substrate and a YBCO gate film), near the depletion a peak appeared showing a capacitance enhancement, surpassing the capacitance at high densities (geometrical limit), $C_{\text{hd}} \approx C_{\text{geom}}$. In addition $d\mu/dn$ measurements fall below zero for low-densities regime. Figure 2.4(b) illustrates this decline.

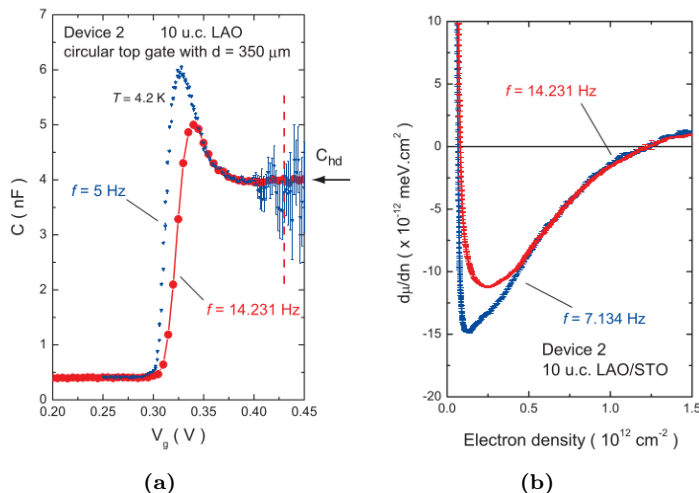


Figure 2.4. Measurements in a capacitor made of a LaAlO_3 10-unit-cells thickness deposited onto the top of TiO_2 -terminated SrTiO_3 substrate and a $350\text{-}\mu\text{m}$ -diameter top gate film. (a) Graphic representation of C versus V_g . The measurements were performed at $T = 4.2 \text{ K}$ and frequencies $f = 5 \text{ Hz}$ in blue and $f = 14.231 \text{ Hz}$ in red [14]. (b) Dependence of the inverse of compressibility, $d\mu/dn$ with respect the electron density n . The selected frequencies have been $f = 7.134 \text{ Hz}$ in blue and $f = 14.231 \text{ Hz}$ in red. Reproduced with permission from [14].

In these conditions, a 40% (with respect the geometrical value) enhancement in the capacitance is observed at low frequencies $f = 5 \text{ Hz}$ (Fig. 2.4(a)). Such considerable amplification in the capacitance has been never obtained, even in high-mobility GaAs-based systems [2]. The enhancement was attributed to the the negative compressibility. Attending to Fig. 2.4(b), there exists a critical electron density below which the electronic compressibility is negative. This phenomenon is observed at low densities regime (of the order of $10^{12} \text{ electrons/cm}^2$).

2.2 CRITICAL ANALYSIS

Kopp and Manhart's model presents the indisputable benefit of its simplicity but is based on a number of assumptions. Here we will like to try to asses its validity to explain the experimental results in $\text{SrTiO}_3/\text{LaAlO}_3$ interfaces.

- In Kopp and Mannhart models, the atomic structure is disregarded. These authors use a jellium background with an homogeneous positive density.
- The formation of a completely two-dimensional electron gas deflects from real systems. Actual confined electron gas possess a finite thickness. Computational calculations in modelled interfaces were developed in Ref. [11] considering a finite width for the 2DEG. The results of this research showed a notable variability in the physical response of different systems, where the geometry, confinement and additional factors play a key role. These variability is a consequence of two electrostatic factors: Hartree band-bending and image charge effects, opposite to Mannhart conclusions where exchange and kinetic contributions would dominate.
- The formation of a free electron gas model might not be the most suitable one in STO/LAO interfaces. However, it can be applied on standard semiconductors (like GaAs and $\text{Al}_x\text{Ga}_{1-x}\text{As}$) where electron gases are formed by quantum well structures as shown in Fig. 2.5(a). The quantum well generation is due to the band bending perpendicular to the interface inducing quantization of the electronic states. Conversely, in the case of SrTiO_3 and LaAlO_3 interface (interfaces between oxides), the two-dimensional electron bands are generated in the

potential wells emerging from the ionic charges since Ti d -orbitals present strong electronic correlations (Fig. 2.5(b)). In the oxide interface, the model of a two-dimensional liquid is more appropriate than the two dimensional gas approach. As consequence, the assumption of the homogeneous electron gas laws for exchange and correlation is not fully supported.



Figure 2.5. Schemes of band diagrams for two dimensional electron systems generated in the interface of two semiconductors, GaAs and $\text{Al}_x\text{Ga}_{1-x}\text{As}$ (a) and two oxides, SrTiO_3 and LaAlO_3 (b). Attending to semiconductors interface, the predominant effect in two dimensional bands is the band bending phenomenon which causes a quantum well in the interface. Otherwise, the electronic subbands in oxide interface are characterized by the potential wells emerging from the ionic charges [17].

2.3 OUR PROPOSAL

Within this work we propose an innovative mechanism to explain the unconventional phenomenon of negative electron compressibility. In an electron gas, the main components to understand the negative compressibility are the following:

- The formation of polarons to localize electrons in the low density regime.
- The relevance of the direct electrostatic interactions between the two electrodes.
- The anisotropy of the dielectric constant of the medium.

Considering $\text{SrTiO}_3/\text{LaAlO}_3$ interface in a low densities regime (where negative compressibility has been discovered experimentally), our model proposed that the electrons would be localized in polarons in SrTiO_3 system. A polaron is a quasiparticle constituted by an electron and a phonon cloud (its additional strain field) [8]. The presence of polarons in SrTiO_3 has been already observe experimentally. However, their measurement is an arduous task. These quasiparticles are very sensitive to octahedral tiltings and correlation effects [7].

Let us assume that we have an electron localized as a polaron. Applying the image charge model on the system, the electron is attracted to the interface electrostatically by its image charge within the metallic electrode on top of the LaAlO_3 . This Coulomb attraction is partially screened by the dielectric constant of the LaAlO_3 ($\epsilon_{\text{LAO}} \approx 24$ at $T = 300$ K [5]). If a second polaron (with the corresponding image charge) approaches, then the Coulomb repulsion between the two polarons will be screened by the dielectric constant of the SrTiO_3 ($\epsilon_{\text{STO}} \approx 300$ at $T = 300$ K [12]). As shown in the Figure 2.6(a) the Coulomb attraction between the polarons and the image charges might compensate screened electrostatic repulsion. In other words, within this model if a pair polaron-image charge is formed the second one would be energetically favourable. It should be stressed, the requirement of lower

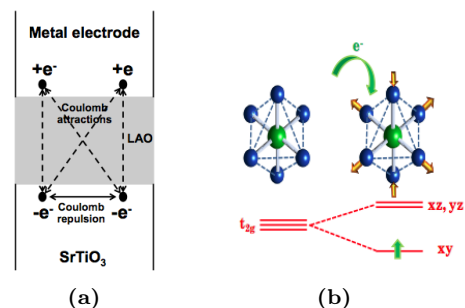


Figure 2.6. (a) Scheme representation of our proposed model based on image charge method. (b) Single electron capture in SrTiO_3 accompanied by lattice distortions.

electronic density regime to observe the manifestation of this phenomenon. Since the addition of one electron leads to lattice distortions, Fig. 2.6(b) (polaron formation), which concerns a elastic energy cost. If the electronic density n is larger than a critical value, the elastic energy proceeding from lattice distortions is not longer compensated by the attractive interactions leaving the negative compressibility effect.

2.4 CHALLENGES

Confronting the computational study of the present problem is impracticable from current state-of-the-art methodologies. The involved theoretical simulations entail several challenges which are beyond the fist principles limits.

- Size of the system. The experimental measurements of capacitance enhancement are observed for electron densities $\sim 10^{12}$ e/cm². This quantity is equivalent to consider one extra electron per a surface 25×25 unit cells of SrTiO₃. As consequence, the study of this phenomenon leads to a huge amount of atoms which is not covered by first principles simulations. Moreover, interfaces present reduced symmetry. This property implies that large unit cells must be utilized, which requires the study of large system.
- Two-materials interface. In addition to the low-symmetry property of an interface, they are complex and heterogeneous. Its complexity arises from the presence of defects and impurities, and the interaction between two different systems. The combination of these phenomenons leads to the prediction of unusual electronic, optical, magnetic, and mechanical properties.
- Electronic correlation. The main feature of the proposed model is the localization of the electrons which suffer high correlation interactions. DFT implementations incorporate exchange and correlation phenomena but in an approximated way being unsuccessful for localized electrons.
- Electron-lattice interactions. As stated above, the essential piece of our model is the formation of polarons in SrTiO₃ substrate which localize the $3d$ electrons. The presence of these pseudoparticles assumes the coupling of a cloud of lattice distortions (phonons) in SrTiO₃ and electrons. The study of the electron-phonon interactions demands perturbative approaches which go a step further of the standard codes implementations.
- Electrostatic effects. Attractive interactions between polarons and the image charges must be included in the simulation.

ELECTRONIC STRUCTURE SrTiO₃

The starting point for any theoretical characterization of the SrTiO₃/LaAlO₃ 2DEG interface is the study of the accommodation of the extra electronic charge. According to the polar catastrophe model, this excess of charge is transferred from the top of the valence band of LaAlO₃ system to the bottom of the conduction band of SrTiO₃. Here we carry out the analysis of the electronic band structure SrTiO₃ making an especial emphasis on precisely those states at the bottom of the conduction band.

3.1 SrTiO₃ BAND DIAGRAM AND PROJECTED DENSITY OF STATES

The Kohn-Sham electronic band structure of SrTiO₃, within the Local Density Approximation (LDA), has been computed in the centrosymmetric cubic paraelectric configuration at the equilibrium lattice constant, $a = 3.874 \text{ \AA}$. The results are shown in Fig. 3.1(a). A mixture of ionic and covalent features are observed:

On the one hand, bands can be separated by energy regions that we call *energy windows*, centered around the energies corresponding to a particular atomic orbital. Each energy window contains a set of J consecutive energy bands that do not become degenerate with any lower or higher band anywhere in the BZ. The windows are sufficiently separated, and the bands within these manifolds are relatively flat, showing that *ionic* behaviour. As consequence, the bands present a dominating character which is identified by the name of the atomic orbital that mainly constitutes this energy state in the solid.

On the other hand, the *covalent* manifestations are observed in the hybridization between O-2*p* and Ti-3*d* orbitals. It is necessary to mention that the four electrons belonging to Ti-3*d* are not totally transferred to oxygen *p*-orbitals, part of the electronic density remains to some extent delocalized in the Ti atom. Moreover, the static charges are smaller than the ones expected in a completely ionic material. In the band diagram this effect is translated in a mixture of Ti-3*d* and O-2*p* characters. For deeper states, an additional significant hybridization between Sr-4*p* and O-2*s* orbitals emerges. Both hybridizations are clearly displayed in Fig. 3.1(b).

Extracting the eigenvalues and eigenfunctions of our simulation, we can project over a desired set of atomic orbitals, characterized by specific quantum numbers, and obtain the spatially resolved projected density of states (PDOS). It is localized in a region of space [23]. The representation of PDOS is displayed in Fig. 3.1(b) where we have projected on O-2*s*, Sr-4*p*, O-2*p*, Ti-3*d* atomic orbitals. Here, the ionic and covalent features discussed above can be easily identified. Firstly, for each manifold there exists a majority contribution of a particular atomic orbital character. Indeed, in the study of the *d*-shell orbitals from Ti, a subdivision is performed based on PDOS localization: for these bands, t_{2g} character $\{d_{xy}, d_{yz}, d_{xz}\}$ and e_g orbitals $\{d_{x^2-y^2}, d_{3z^2-r^2}\}$ are decoupled. Secondly, the small covalent phenomena emerge in a faint hybridization in O-2*p* and Ti-3*d* orbitals, and between O-2*s* and Sr-4*p* functions.

Compiling the previous comments and fitting band diagram, Fig. 3.1(a), with projected density of

states, Fig. 3.1(b), the character of the top of the valence band is discernibly O-2p (in blue) despite covalent details exposed previously. Whereas, the bottom of the conduction band is marked by Ti-3d character. The splitting of d -orbitals between t_{2g} and e_g states is due to crystal field splitting and the covalency effects between Ti-3d and O-2p orbitals. The e_g orbitals (in magenta) are pushed up several electron-volts above the t_{2g} orbitals (in green). The obtained energy gap from this LDA calculation is $E_g^{\text{LDA}} = 2.0124$ eV which is subestimated with respect the experimental value, measured by spectroscopic ellipsometry, which amounts to $E_g^{\text{exp}} = 3.25$ eV [24]. Finally, semi-core orbitals of Sr are identified with 4p states (orange) and oxygen core O-2s functions (red).

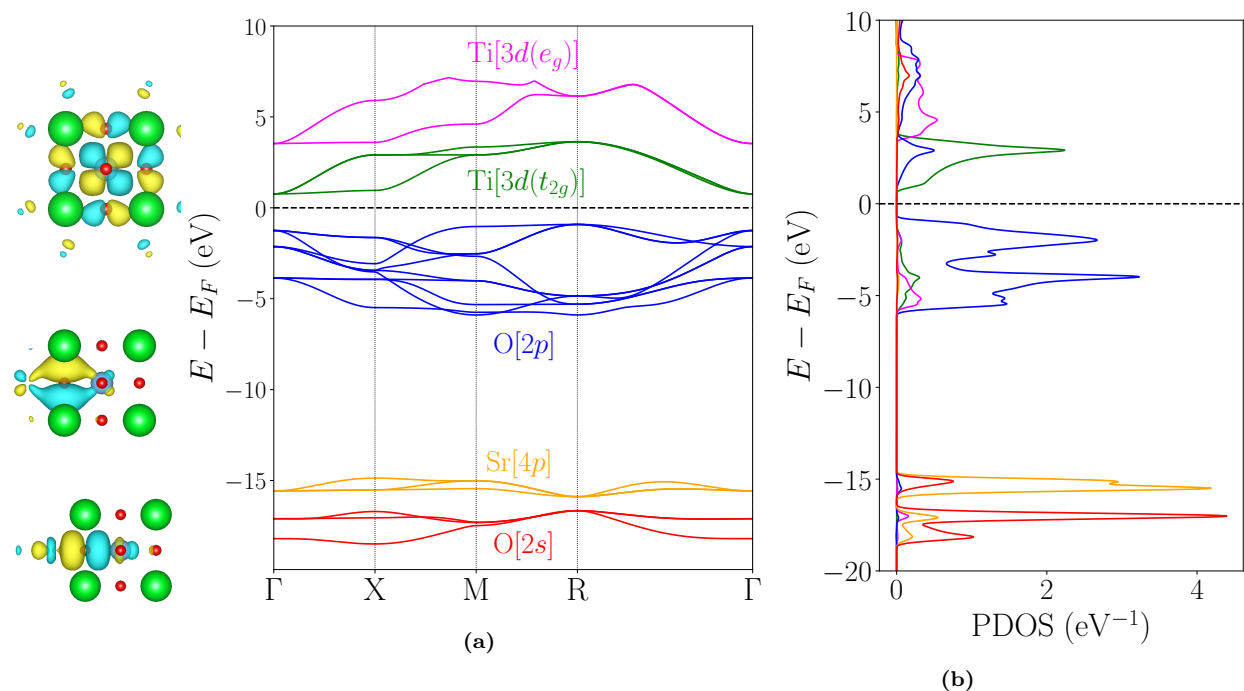


Figure 3.1. (a) Band structure of the SrTiO₃ in the cubic structure at the equilibrium lattice constant. Diagram displays semi-core bands (O-2s in red and Sr-4p in orange), valence band (O-2p in blue) and conduction band (Ti-3d in green for t_{2g} states and in magenta for e_g states). Fermi energy level has been translate to energies origin. (b) Projected density of states of SrTiO₃ in cubic structure at the equilibrium lattice constant. The projections on the O-2s (red), O-2p (blue), Ti- t_{2g} (green), Ti- e_g (magenta) and semi-core Sr-4p (orange) are represented. On the left, two Wannier orbitals are shown for the top of the valence band and a Wannier orbital associated with the bottom of the conduction band is considered.

3.2 WANNIER FUNCTIONS

The electronic structure exposed above is based on the Bloch orbitals, which are the eigenfunctions of the Schrödinger equation. By construction, they are delocalized and span on over all the space. They are also orthogonal and can be considered as a basis of our Hilbert space. The Bloch functions are not univocally defined due to its dependence on an arbitrary phase. To determine them perfectly, we can choose a smooth and periodic gauge [25].

In order to find localized functions in the real space storing the same information as the Bloch basis set, the Fourier transform is applied. The Fourier-transform partners of the Bloch functions are known as Wannier functions which represents a basis set of the Hilbert space too. For the sake of simplicity, we are going to consider the case of one isolated band, meaning that the band never crosses the bands above or below it. Taking the Bloch function $\psi_{m\vec{k}}$ linked to the m index band and wave vector \vec{k} , and the Wannier function labeled by a cell index \vec{R}_n and a band-like index n ,

$\chi_{n\vec{R}}$, we can go from reciprocal space to real space by

$$|\chi_{n\vec{R}}\rangle = \frac{V_{\text{cell}}}{(2\pi)^3} \int_{\text{BZ}} d\vec{k} e^{-i\vec{k}\cdot\vec{R}} |\psi_{m\vec{k}}\rangle, \quad (3.1)$$

and from real space to reciprocal one computing

$$|\psi_{m\vec{k}}\rangle = \sum_{\vec{R}} e^{-i\vec{k}\cdot\vec{R}} |\chi_{n\vec{R}}\rangle. \quad (3.2)$$

This is a special case of a unitary transformation where V_{cell} is the volume of the primitive unit cell and the integral is defined in the Brillouin zone (BZ). The use of the Fourier transform reproduces the periodicity of the crystal since it makes the Wannier functions translational images of one another, as displayed in Fig. 3.2. Summarizing, we can view the Bloch and Wannier functions as providing two different basis sets describing the same manifold of states associated with the electronic band in question.

The Wannier functions are strongly non-unique as a consequence of the phase indeterminacy of Bloch orbitals commented previously. To identify a determined set on the Wannier functions construction in an insulator, a well-defined localization criterion is employed: “maximal localization criterion” [19]. This method consists in the minimization of a localization functional Ω , which measures the sum of the quadratic spreads around their centers defining the Wannier functions at the origin, $\vec{R}_n = 0$,

$$\Omega = \sum_n \left[\langle \chi_{n\vec{0}} | r^2 | \chi_{n\vec{0}} \rangle - \langle \chi_{n\vec{0}} | \vec{r} | \chi_{n\vec{0}} \rangle^2 \right] = \sum_n \left[\langle r^2 \rangle_n - \vec{r}_n^2 \right]. \quad (3.3)$$

The second moment (spread) of the Wannier orbital is determined by the first integral while the second term represents the Wannier center.

Among the properties of the Wannier functions in the single band case, we can stand out the following:

- The Wannier functions are localized in real space, that is

$$|\chi_{n\vec{R}}(\vec{r})| \rightarrow 0 \text{ as } |\vec{r} - \vec{R}| \text{ gets larger.} \quad (3.4)$$

As result, they are perfect to generate range-limited models.

- The Wannier functions are translational images of one another

$$\chi_{n\vec{R}}(\vec{r}) = \chi_{n\vec{0}}(\vec{r} - \vec{R}). \quad (3.5)$$

Or more formally

$$|n\vec{R}\rangle = T_{\vec{R}} |n\vec{0}\rangle \quad (3.6)$$

where $T_{\vec{R}}$ is the operator that translates the system by a lattice vector \vec{R} .

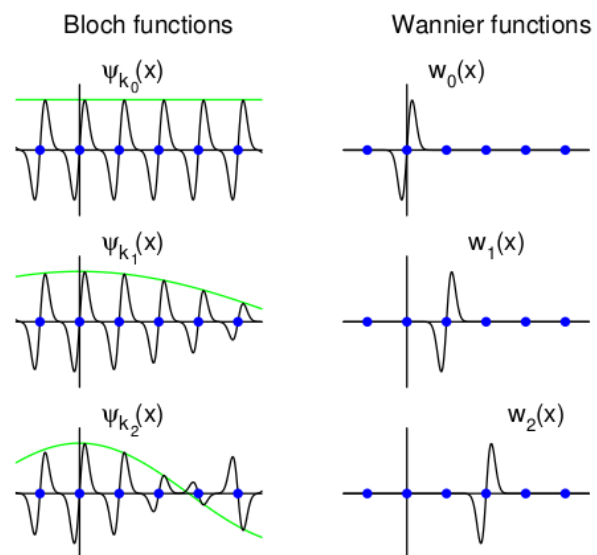


Figure 3.2. Bloch and Wannier functions for a chain of atoms in 1D (blue dots). Left: Bloch functions of a single band for three different values of k . The green curves show the envelopes e^{ikx} of the Bloch functions. Right: Wannier functions obtained for the same band, producing periodic images of one another [18].

- The Wannier functions form an orthonormal basis set,

$$\langle \chi_{n\vec{R}'} | \chi_{n\vec{R}} \rangle = \delta_{\vec{R}'\vec{R}}. \quad (3.7)$$

- The Wannier functions span the same subspace of the Hilbert space as is spanned by the Bloch functions from which they are constructed. Let \mathcal{P}_n be the projector operator onto band n then this can be expressed as

$$\mathcal{P}_n = \frac{V_{\text{cell}}}{(2\pi)^3} \int_{BZ} |\psi_{n\vec{k}}\rangle \langle \psi_{n\vec{k}}| d^3k = \sum_{\vec{R}} |\chi_{n\vec{R}}\rangle \langle \chi_{n\vec{R}}|. \quad (3.8)$$

From this it follows that the total charge density $\rho_n(\vec{r})$ in band n is the same when computed in every representation,

$$\rho_n(\vec{r}) = -e \langle \vec{r} | \mathcal{P}_n | \vec{r} \rangle = -e \frac{V_{\text{cell}}}{(2\pi)^3} \int_{BZ} |\psi_{n\vec{k}}(\vec{r})|^2 d^3k = -e \sum_{\vec{R}} |\chi_{n\vec{R}}(\vec{r})|^2. \quad (3.9)$$

All the equations and properties below can be generalized to the case of isolated band manifolds.

COMPUTATIONAL METHODS

The final goal of this research is focused on the simulation of polarons. In order to carry out these calculations, it is required the coupling between the electronic structure and the lattice, which leads to the implementation of a huge amount of atoms. First principles are only applicable to structures with hundreds of atoms (spatial scales of a few angstroms) and for short periods of time (a few femtoseconds), as consequence, the proposed computational simulations in this work are prohibitive. It is convenient to develop procedures based on first principles that allow the study of this type of systems and much more efficient from the computational point of view. To address these problems the second principles arise, capable of solving problems with hundreds of thousands of atoms.

4.1 BAND DIAGRAM FROM FIRST PRINCIPLES CALCULATIONS

The band diagram of a system is a crucial representation to study its electronic properties. From first principles calculations, the n th band is characterized by the Bloch wave function $\psi_n(\vec{k})$ and its associated energy is $E_n(\vec{k})$, where \vec{k} belongs to the first Brillouin Zone (BZ) [25].

In order to obtain the energies $E_n(\vec{k})$, the following secular equation must be solved,

$$\det \left[H(\vec{k}) - E_n(\vec{k})S(\vec{k}) \right] = 0. \quad (4.1)$$

Here, $H(\vec{k})$ represents the Hamiltonian matrix of the system and $S(\vec{k})$ the overlap matrix, both defined for a \vec{k} point in the BZ. They are square matrices whose dimension is the number of orbitals in the unit cell, $N_{\text{orb/cell}}$, which compose the basis set of our problem. The elements of the Hamiltonian matrix are computed by

$$H_{\mu\nu}(\vec{k}) = \sum_{\vec{R}} e^{i\vec{k}\vec{R}} H_{\mu\nu}(\vec{R}), \quad (4.2)$$

and the ones for the overlap matrix

$$S_{\mu\nu}(\vec{k}) = \sum_{\vec{R}} e^{i\vec{k}\vec{R}} S_{\mu\nu}(\vec{R}). \quad (4.3)$$

Indices μ and ν run over atomic orbitals in the basis set. For the computation of the Hamiltonian and overlap matrices in real space we shall assume that orbital μ is located at the home unit cell ($\vec{R} = 0$), while orbital ν is located in a periodic replica whose translational vector is determined by \vec{R} . Label μ is a contracted notation that encompasses the index of the atom in the unit cell, the angular and the magnetic quantum numbers and any other possible indexes required to characterized the atomic orbital.

In *ab-initio* calculations the matrix elements $H_{\mu\nu}(\vec{R})$ and $S_{\mu\nu}(\vec{R})$ are computed from first principles by

$$H_{\mu\nu}(\vec{R}) = \left\langle \phi_{\mu}(\vec{r} - \vec{R}') \left| H \right| \phi_{\nu}(\vec{r} - [\vec{R}' + \vec{R}]) \right\rangle = \left\langle \phi_{\mu}(\vec{0}) \left| H \right| \phi_{\nu}(\vec{R}) \right\rangle \quad (4.4)$$

and

$$S_{\mu\nu}(\vec{R}) = \left\langle \phi_{\mu}(\vec{r} - \vec{R}') \middle| \phi_{\nu}(\vec{r} - [\vec{R}' + \vec{R}]) \right\rangle = \left\langle \phi_{\mu}(\vec{0}) \middle| \phi_{\nu}(\vec{R}) \right\rangle. \quad (4.5)$$

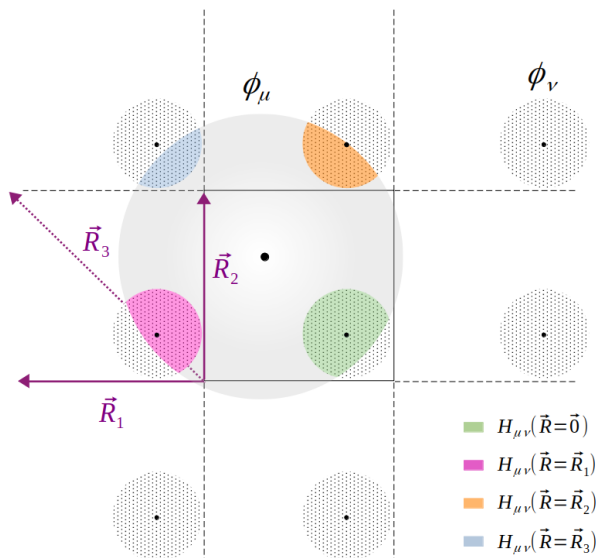


Figure 4.1. Interactions between an orbital placed at the home unit cell, ϕ_{μ} , and the periodic images of another orbital ϕ_{ν} . The Hamiltonian matrix elements will be null if there is not overlap between the orbitals.

The proper description of the electronic band structure usually requires the consideration of many atomic orbitals. For instance, in the case of SrTiO_3 , as shown in Fig. 3.1(a), we need to include all the valence orbitals of atoms O, Sr and Ti and even the semi-core states for the metallic cations. This is translated into the fact that for every unit cell considered in our problem we need to include of the order of 72 bands per unit cell. The simulation of a $2 \times 2 \times 2$ super cell requires the diagonalization of matrices of dimension 576. Since the computational cost of the diagonalization scales as $O(N_{\text{orb/cell}}^3)$ we can ascertain how the first principles treatment of the super cells to simulate a polaron is unfeasible.

4.2 TIGHT BINDING IN WANNIER FUNCTIONS

As it was said before, the band structure can be described in a basis of Wannier functions. Indeed, it can be proved that

$$\langle \chi_{n\vec{0}} | H | \chi_{n\vec{R}} \rangle = E_n(\vec{R}), \quad (4.6)$$

so the diagonal elements between Wannier functions are the coefficients in the Fourier expansion of the band energy,

$$E_n(\vec{R}) = \frac{V_{\text{cell}}}{(2\pi)^3} \int_{BZ} e^{-i\vec{k}\vec{R}} E_{n\vec{k}} d^3k. \quad (4.7)$$

For the sake of simplicity, we assume again the case of isolated bands, but this expression can be generalized to the study of a band manifold. From a practical point of view, these matrix elements can be obtained from the knowledge of the band structure, the k -points sampling and the volume of the unit cell, V_{cell} . These operations are done within the WANNIER-90 code. Deeming a physical perspective, Eq. (4.6) represents the same matrix elements in real space as shown in Fig. 4.1, but in a basis of Wannier functions and not in atomic orbitals. Then, applying the inverse Fourier transform we can compute the band structure in the reciprocal space knowing the Hamiltonian

matrix elements written in a basis of Wannier functions,

$$E_n(\vec{k}) = \sum_{\vec{R}} e^{i\vec{k}\cdot\vec{R}} E_n(\vec{R}). \quad (4.8)$$

Analysing Eq. (4.8), it is formally the same as the Hamiltonian matrix expressed in a basis of Bloch-like basis functions, Eq. (4.2). In other words, the Wannier functions provide an exact tight-binding representation of the dispersion $E_n(\vec{k})$ of band n where tight binding on-site energy is obtained by $E_n(\vec{R} = 0)$ and the hoppings are given by $E_n(\vec{R})$ to its neighbour located at \vec{R} .

Equation (4.8) is exact and by construction we reproduce the band dispersion.

- Since the Wannier functions are localized, the hopping matrix elements decay rapidly with distances, so that a few hoppings are typically retained,

$$E_n(\vec{k}) \approx \sum_{\|\vec{R}\| < \delta r_n} e^{i\vec{k}\cdot\vec{R}} E_n(\vec{R}) \quad (4.9)$$

where δr_n is a radius cutoff designed as *cutoff-h*. This approximation is systematically convergent. In order to obtain a better representation of the band diagram, the increasing of the δr_n value is enough being the asymptotically limit of the bands the ones obtained by the Bloch orbitals.

- Second important point is that we can restrict our bands to the treatment of the set of active electrons in our problem. That means we can wannierize and keep in our calculations only the bands that really play a role in the physical problem under study. In the case of the polaron existence which we are interested in, it will be enough to keep the *top-valence* and the *bottom-conduction* bands related to the O $2p$ and Ti t_{2g} characters respectively. This leads to a tight binding model integrated by 12 bands per unit cell, in contrast to first principles calculations, performed with 72 bands per unit cell, arising a high reduction of the computational cost.
- Until now, we have worked on the isolated band treatment. However, bands can display nonanalytic behaviours as crossings with other bands and singularities. This is the difficulty observed in the active set of our system. To solve this problem, we left the notion of isolated bands and we consider multiband *manifolds* defined as a set of J consecutive energy bands that do not become degenerate with any lower or higher band anywhere in the Brillouin zone (energy window concept described above). Well localized Wannier functions can still be constructed if we abandon the idea that each Wannier function should be associated with one and only one energy band. At this point, the Wannier orbital set $|\chi_{n\vec{R}}\rangle$ represents each one of the J bands composing a manifold and spans the same subspace as the Bloch functions $|\psi_{n\vec{k}}\rangle$ considered as a group, $|\tilde{\psi}_{n\vec{k}}\rangle$. For example, in SrTiO₃ $n = 1, \dots, 9$ which composed the top of the valence band manifold while $n = 1, 2, 3$ represent the bottom of the conduction band manifold,

$$|\chi_{n\vec{R}}\rangle = \frac{V_{\text{cell}}}{(2\pi)^3} \int_{BZ} d\vec{k} e^{-i\vec{k}\cdot\vec{R}} |\tilde{\psi}_{n\vec{k}}\rangle. \quad (4.10)$$

The new Bloch-like wave functions $|\tilde{\psi}_{n\vec{k}}\rangle$ are smooth functions of \vec{k} everywhere in the BZ and they are related to the true (energy-eigenstate) wave functions via a unitary transformation $U_{mn}(\vec{k})$ for each \vec{k} in the BZ,

$$|\tilde{\psi}_{n\vec{k}}\rangle = \sum_{m=1}^J U_{mn}(\vec{k}) |\psi_{m\vec{k}}\rangle. \quad (4.11)$$

And instead of Eq. (4.8), we compute the energies solving the secular equation

$$\det [H_{mn}(\vec{k}) - E_n(\vec{k})] = 0. \quad (4.12)$$

The terms $H_{mn}(\vec{k})$ represent the matrix elements of a $J \times J$ Hamiltonian matrix constructed as

$$H_{mn}(\vec{k}) = \sum_{\vec{R}} e^{i\vec{k}\vec{R}} H_{mn}(\vec{R}) \quad (4.13)$$

where

$$H_{mn}(\vec{R}) = \langle \chi_{m\vec{0}} | H | \chi_{n\vec{R}} \rangle. \quad (4.14)$$

The equality $H_{mn}(\vec{k}) = \langle \tilde{\psi}_{n\vec{k}} | H | \tilde{\psi}_{m\vec{k}} \rangle$ is fulfilled. Equivalently with Eq. (4.9) a δr_h cutoff can be applied,

$$H_{mn}(\vec{k}) \approx \sum_{\|\vec{R}\| < \delta r_h} e^{i\vec{k}\vec{R}} H_{mn}(\vec{R}). \quad (4.15)$$

- From the point of view of the band manifold study, the Wannier functions maintain the orthonormality already expressed in the isolated band case, Eq. (3.7). As result, for a basis set composed by Wannier functions the overlap matrix S is the identity,

$$S(\vec{R}) = \langle \chi_{n\vec{R}'} | \chi_{m\vec{R}} \rangle = \delta_{\vec{R}'\vec{R}} \delta_{nm}. \quad (4.16)$$

This section has been elaborated according to the Ref. [25].

4.3 PARAMETRIC ONE-ELECTRON HAMILTONIAN

As discussed above, the electronic band structure of a system can be computed by a simple tight binding model, Eq. (4.15). This model presents several advantages, as the low computational cost and the high efficiency. The main ingredient for its application are the Hamiltonian matrix elements expressed in the Wannier functions basis set, $H_{nm}(\vec{R})$ shown in Eq. (4.15). Thus, now, the objective we aim to achieve is the construction of these matrix elements parametrically. From first-principles simulations, we want to obtain tight binding parameters that are flexible enough to describe different atomic configurations and distinct electronic states beyond the Born-Oppenheimer surface.

To describe the atomic and electronic configuration of the system we shall adopt a notation similar to that of Ref. [10]. The magnitudes related to the atomic structure will be labeled by Greek letters. Considering periodic three dimensional infinite crystal, the different cells are denoted by uppercase letters $\{\Lambda, \Delta, \dots\}$ and the corresponding atoms in the cell as lowercase letters, $\{\lambda, \delta, \dots\}$. According to this, the lattice vector of the cell Λ is \vec{R}_Λ . In order to employ a more compact notation, a cell/atom pair shall be represented as a bold lowercase index, i.e., $\vec{R}_\Lambda \lambda \leftrightarrow \boldsymbol{\lambda}$. The elements related to electrons are labeled by Latin subindices. In particular, the Wannier functions will group both the cell and its discrete label in a contracted bold index $\boldsymbol{a} \leftrightarrow \vec{R}_\Lambda a$.

Any possible crystal configuration can be specified by expressing the atomic positions, \vec{r}_λ , as a distortion with respect a RAG as

$$\vec{r}_\lambda = (\mathbb{1} + \overleftrightarrow{\eta}) (\vec{R}_\Lambda + \vec{\tau}_\lambda) + \vec{u}_\lambda, \quad (4.17)$$

where $\mathbb{1}$ is the identity matrix, $\overleftrightarrow{\eta}$ is the homogeneous strain tensor, and \vec{u}_λ is the absolute displacement of atom λ in cell Λ with respect to the strained reference structure.

This section has been written according to the Ref. [10].

4.3.1 Reference state Hamiltonian

The starting point of our method relies on the following key concept: the reference atomic geometry (RAG). As in the recent development of model potentials for lattice-dynamical studies [27], the

first step towards the construction of our model is the choice of a RAG, that is, one particular configuration of the nuclei that we will use as a reference to describe any other configuration. In principle, no restrictions are imposed on the choice of the RAG. However, it is usually convenient to employ the ground state structure or, alternatively, a suitably chosen high-symmetry configuration. Note that these choices correspond to critical points of the PES, so that the corresponding forces on the atoms and stresses on the cell are zero. Further, the higher the symmetry of the RAG, the fewer the coupling terms needed to describe the system and, in turn, the number of parameters to be determined from first principles [10].

Returning to our system, the selected RAG is the SrTiO₃ in the cubic phase. This lattice represents a high-symmetry configuration and it allows the generation of other configurations by small lattice distortions.

Once the reference geometry has been defined, we focus on the Hamiltonian construction. The real space one-electron Hamiltonian terms $h_{\mathbf{ab}}$ represents the *interaction* between the Wannier functions $\chi_{\mathbf{a}}$ and $\chi_{\mathbf{b}}$, where each one of them describes a given band and is centered in a certain atom due to the rather ionic character of SrTiO₃ system. These Wannier functions have been constructed following a *wannierization* procedure. The first step consists of selecting the manifolds we want to express in a basis of Wannier functions, i.e., the active set. According to the problem we are interested in, the active set is composed by two manifolds: the top of the valence band dominated by the O 2*p* bands (shown in blue in Fig. 3.1(a)) and the bottom of the conduction band related to the Ti *t*_{2*g*} bands (colored in green). Employing WANNIER-90 code, the transformation of Eq. (4.10) is performed expressing Bloch functions as Wannier orbitals. Some of the obtained Wannier functions for this problem are shown on the left of the Fig. 3.1. In addition, from these Wannier functions, WANNIER-90 code also generates the $H_{mn}(\vec{R})$ matrix elements expressed in Eq. (4.14). These Hamiltonian matrix elements corresponds to the one-electron matrix elements of the usual tight binding model in the RAG. Recovering the current Wanniers notation, $\gamma_{\mathbf{ab}}^{\text{RAG}}$.

Then, as first stage, the Hamiltonian matrix elements of our parametric model are the $\gamma_{\mathbf{ab}}^{\text{RAG}}$ variables,

$$h_{\mathbf{ab}}^s = \gamma_{\mathbf{ab}}^{\text{RAG}}. \quad (4.18)$$

A. Electronic band structures

The previous Hamiltonian is able to reproduce the bands of the RAG geometry. In Fig. 4.2 we superimpose the band diagram obtained for the SrTiO₃ system from full first principle calculations-employing DFT by SIESTA software- displayed in blue, and by the developed models based on Eq. (4.18) obtained varying $\delta r_h \in \{6 \text{ \AA}, 8 \text{ \AA}, 10 \text{ \AA}\}$, in red. On the top of the diagrams are shown the corresponding value for this cutoff and the number of one electron interactions in the resulting models (it is clear diagonal elements are always included regardless the selected value). Employing these values, it is possible to evaluate the size of the model and estimate the computational cost required to attain an adequate representation of the band structure of a system.

The cutoff distance δr_h determines the retained Hamiltonian matrix elements $h_{\mathbf{ab}}$, i.e., it selects the Wannier function interaction pairs (\mathbf{a}, \mathbf{b}) which will be considered. Changing δr_h , bands calculation can be improved systematically. Attending to Fig. 4.2 bands fit better to first principles bands the higher the cutoff number.

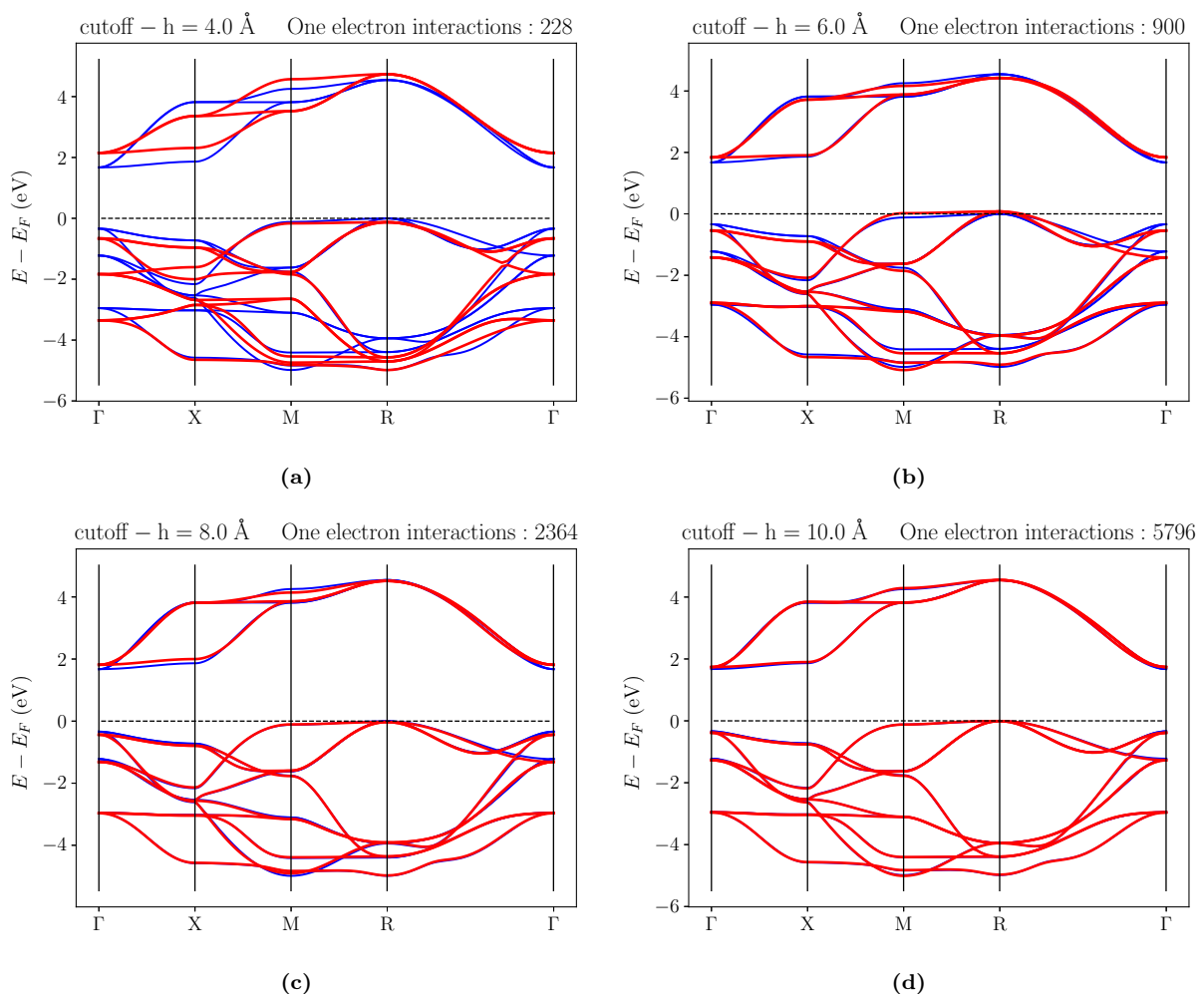


Figure 4.2. Representation of the bands of SrTiO₃ for various values of the distance cutoff δr_h . Blue lines represent the bands obtained from first principles, while the results from the second-principles model are shown in red. On top of each plot we indicate the corresponding number of h_{ab} matrix elements per unit cell that are included.

4.3.2 Interaction groups

The crystalline solids are characterized by their symmetry, reflected by their point and space groups. In particular, we are interested in the SrTiO₃ system, whose space group is Pm-3m. Clearly, the interactions in our system, h_{ab} , shall be related by the symmetry operations of the spatial group. In order to consider the symmetry of the system in the building Hamiltonian, we collect all the equivalent interactions by symmetry in a same group. These groups will be called *interaction groups*. Following this reasoning, the interactions h_{ab} and $h_{a'b'}$ will belong to the same interaction group if there exists a symmetry operation $\hat{T} \in \text{Pm-3m}$ such that

$$\hat{T}h_{ab} = h_{a'b'}. \quad (4.19)$$

For example, we consider the interaction between the Wannier function d_{xz} -like centered in the Ti atom (Wannier function denoted as \mathbf{a}) and the Wannier function p_z -like in O₁, on the same plane as the Ti atom (Wannier function named by \mathbf{b}) and both in the unit cell. This interaction is denoted as h_{ab} and is shown in Fig. 4.3(a), where the blue lobes represent the positive values while the red lobes the negative ones. Now, we study the interaction between the previous Wannier function \mathbf{a} and the Wannier function p_x -like in O₂ (associated with the label \mathbf{c}) shown in Fig. 4.3(b). In

this case, the interaction is designed as h_{ac} . It is clear the h_{ac} interaction is equal to the h_{ab} interaction: the lobes with the same colors are faced. Indeed, h_{ab} and h_{ac} are related by the function composition of two operations belonging to the SrTiO₃ space group Pm-3m: a reflection plane m in the xy -plane which crosses through the center of the Wannier functions and a C_4 rotation axis (90-degree counterclockwise) placed on the Ti atom and directed in the y -axis,

$$(C_4 \circ m)h_{ab} = h_{ac}. \quad (4.20)$$

Here, we can see h_{ab} and h_{ac} are equivalent interactions related by the symmetry operation $C_4 \circ m$.

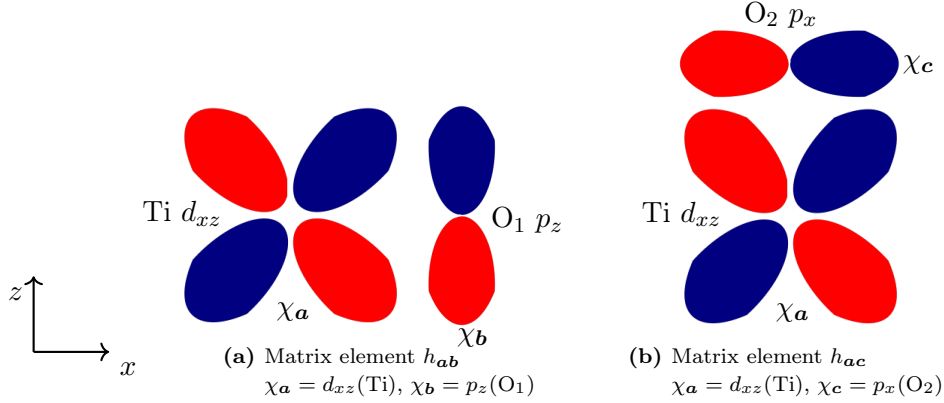


Figure 4.3. Equivalent interactions between two Wannier functions of the SrTiO₃ system: (a) Ti- d_{xz} with O₁- p_z and (b) Ti- d_{xz} with O₂- p_x . These interactions belong to the same *interaction group* since they are equivalent under a symmetry operation of the SrTiO₃ space group.

As result, it is possible to work with the different groups instead of each individual interaction, leading to a reduction of the degrees of freedom. This brings on the construction of a model with a smaller amount of parameters entailing a lowering of the computational demand. For instance, Tab. 4.1 collects the number of interactions and interaction groups selecting different values for the δr_h . For example, we bounce from 900 elements to 31 for $\delta r_h = 6.0 \text{ \AA}$.

δr_h (Å)	# Interactions (h_{ab})	# Groups
4.0	228	15
6.0	900	31
8.0	2364	58
10.0	5796	118

Table 4.1. Number of interactions and number of interaction groups for SrTiO₃ models differentiated by the value of δr_h .

4.3.3 Electron-lattice Hamiltonian

ABO₃ systems are prone to antiferrodistortive (AFD) phases (tilting and rotation along the z -axis of the oxygen octahedra surrounding the B cation are produced, generating a small deformation of the unit cell leading to a tetragonal lattice); ferroelectric (FE) phases (off-center cooperative effect characterized by the opposite displacement of the cations with respect to the O cage, arising parallel dipoles in cells) and antiferroelectric (AFE) phases (characterized by ferroelectric distortions which produce antiparallel dipoles). Electronic band structure of SrTiO₃ from these distorted geometries (with respect the cubic phase selected as RAG) can't be reproduced by the Hamiltonian in Eq. (4.18). Modifications in geometry translate into changes in bonds and orbital hybridisations.

Then, to generate a Hamiltonian which captures all these possible geometry perturbations, electron-lattice coupling corrections, $\delta\gamma_{ab}^{\text{ellat}}$ are introduced. As result,

$$h_{ab} = \gamma_{ab}^{\text{RAG}} + \delta\gamma_{ab}^{\text{ellat}}. \quad (4.21)$$

In order to study how the electron-lattice correction changes with the atomic geometry, the lattice can be deformed by two different ways. On the one hand, lattice can be distorted following some well defined modes based on the desired geometry from which we want to calculate the band diagram (ferroelectric phase, antiferrodistortive phase, ...). However, many calculations are required and the only relevant modes are not known before hand. Furthermore, this model shall just determine the bands when we start from the selected geometry. On the other hand, based on the RAG geometry, randomly distortions are applied generating random structures, which can be expressed as a linear combination of normal modes. So, all the modes are activated and the model will be able to reproduce the electronic band structure of whichever geometry. This is the method of choice here: a set of calculations, called *the training set* (TS), is performed to get the electron-lattice terms.

A. Electron-lattice training set

For the purpose of generating the electron-lattice training set $\{A^{\text{ellat}}\}$, we run a collection of configurations from first-principles calculations in a super cell $2 \times 2 \times 2$ geometry- while ferroelectric phase can be studied in the unit cell, the simulation of the rotations in an antiferrodistortive system needs a super cell geometry - keeping a reasonably computational efficiency. The distortions consist on random movements of the atoms around its reference position in a sphere of a selected radius and characterized by a uniform distribution. For each calculation included in the training set, the Hamiltonian matrix elements in a basis of Wannier functions, $H_{mn}(\vec{R})$ are computed with WANNIER-90, code.

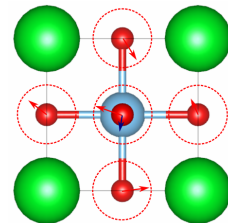


Figure 4.4. Random displacements of O and Ti atoms around a sphere to generate calculations for the training set.

B. Electron-lattice terms

As shown in Ref. [10], electron-lattice terms $\delta\gamma_{ab}^{\text{ellat}}$ can be written as expanded in a Taylor series on distortions of the atomic geometry (i.e. we assume that the deformations are relatively small)

$$\delta\gamma_{ab}^{\text{ellat}} = \sum_{\lambda\nu} \left[-\vec{f}_{ab,\lambda\nu}^T \delta\vec{r}_{\lambda\nu} + \sum_{\lambda'\nu'} \delta\vec{r}_{\lambda\nu}^T \overleftarrow{g}_{ab,\lambda\nu\lambda'\nu'} \delta\vec{r}_{\lambda'\nu'} + \dots \right], \quad (4.22)$$

where

$$\delta\vec{r}_{\lambda\nu} = \overleftarrow{\eta} \left(\vec{R}_\Upsilon - \vec{R}_\Lambda + \vec{\tau}_\nu - \vec{\tau}_\lambda \right) + \vec{u}_\nu - \vec{u}_\lambda \quad (4.23)$$

quantifies the relative displacement of atoms λ and ν . In addition, \vec{f} and \overleftarrow{g} are the first- and second-rank tensors that characterize the electron-lattice coupling, closely related to the concept of *vibronic constants*. These terms influence on the electronic structure modulating the electrostatic interactions in several ways. In order to understand the physics of the \vec{f} terms we study the following particular cases:

◦ **Diagonal interactions, h_{aa} .** The interaction h_{aa} controls the average energy (center of mass) of the corresponding band. Hereunder, we separate the effect produces by the lattice on the electrons, and the alterations generated by the electrons in the lattice.

From the lattice to electrons: the parameters depend on the underlying geometry

This interaction is related to $f_{aa,\lambda\nu}^T$ terms. If $f_{aa,\lambda\nu}^T \neq 0$, then a relative displacement between two atoms, $\delta\vec{r}_{\lambda\nu}$, might modify the center, shape and spreading of the Wannier χ_a , and therefore the center of gravity of the bands. An example is illustrated in Fig. 4.5(a). It shows a p_x and a p_y -like Wannier orbitals and the presence of forces applied on atoms (spheres). If atoms are displaced along the x -direction, a change in the on-site energy of the p_x orbital is produced. In Fig. 4.5(a) we have assumed positive value of the $f_{aa,\lambda\nu}^T$ parameter. As result, the energy of the p_x orbital is lowered while the energy of p_y does not change.

From the electrons to lattice: the forces depend on the electronic density

The force which suffers an atom λ is computed by

$$\vec{F}_\lambda = -\vec{\nabla}_\lambda E = -\vec{\nabla}_\lambda E^{(0)} - \sum_{ab} D_{ab}^U \vec{\nabla}_\lambda \gamma_{ab}. \quad (4.24)$$

The term of the deformation occupation matrix, D_{ab}^U , quantifies the difference between the density matrix and the reference density matrix (RED), which use to be identify with the ground state density of the neutral system (this concept will be further explained in Sec. 4.3.4). Then, if the occupation of a particular Wannier χ_a is changed by the injection of extra charge or by charge extraction, the matrix element $D_{aa}^U \neq 0$ and we are out of Born-Oppenheimer surface. The modification of the occupation can induce atomic forces on atom λ , Fig. 4.5(b), and therefore a displacement. As result, the force field is corrected by the second term in Eq. (4.24). In our model, these distortions are included in \vec{f}_{aa} .

◦ **Off-diagonal interactions, h_{ab} .** The non-diagonal h_{ab} one-body terms control the hopping (i.e. the hybridization, covalency, and the width of the bands).

Here, we take into account the $f_{ab,\lambda\nu}^T$ elements. If $f_{ab,\lambda\nu}^T \neq 0$, then a relative displacement between two atoms $\delta r_{\lambda\nu}$ might modify the overlap between the Wannier functions χ_a and χ_b , and therefore the hopping terms. In other words, \vec{f} measures the alteration in the bandwidths with the atomic displacements. The picture in Fig. 4.5(c) displays the interaction between two orbitals (Wannier functions χ_a centered in atom λ and χ_b centered in atom ν) when the atoms where are located move. Considering the displacements \vec{u}_λ and \vec{u}_ν distancing the two atoms, the Wannier functions shall get farther decreasing its overlap and then, the hopping. As result, the bandwidth becomes narrower (in green) with respect the absence of distortion (in red).

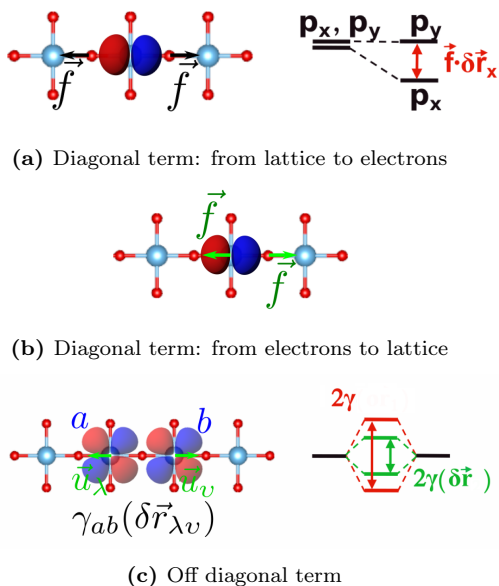


Figure 4.5. Examples of electron-lattice coupling effects. The diagonal term $f_{aa,\lambda\nu}^T$ produce a reduction of the on-site energy of a p_x orbital when a displacement on the x -direction is applied, (a) and the modification of the occupation of Wannier orbitals can induce atomic force in the neighbour atoms, (b). The off-diagonal term $f_{ab,\lambda\nu}^T$ generates alterations on the bandwidth when there is a relative displacement between atoms and thus, between orbitals, (c). In the picture we have neglected the Sr atoms since it does not participate in the active set.

The quadratic terms \overleftarrow{g} are typically much smaller than the linear ones. In addition, among the quadratic constant, the off-diagonal terms use to be negligible with respect the diagonal elements,

$$\overleftarrow{g}_{ab,\lambda\nu\lambda'\nu'} \approx \overleftarrow{g}_{ab,\lambda\nu\lambda'\nu'} \delta_{\lambda\lambda'} \delta_{\nu\nu'} = \overleftarrow{g}_{ab,\lambda\nu}. \quad (4.25)$$

In the MODELMAKER language, $\vec{f}_{ab,\lambda\nu}$ and $\overleftarrow{g}_{ab,\lambda\nu}$ are electron-lattice *terms* or *parameters* which modify a h_{ab} interaction. And a pair $\{\vec{f}_{ab,\lambda\nu}, \overleftarrow{g}_{ab,\lambda\nu}\}$ is an electron-lattice *variable*.

C. Electron-lattice cutoffs

The construction of an actual model involves several approximations as the spatial range of interaction or the number of integrated Wannier functions, inter alia. Here, we are focused on the generation of a model able to reproduce the first principles calculation of the training set reaching a balance between accuracy and efficiency. Originally, this scheme contains all the possible electron-lattice terms: we can fit the model recreating the one-electron Hamiltonian of the constructed electron-lattice training set with accuracy. However, we need to simplify it. Trying different combinations of parameters we identify the strongest and most relevant interactions. For example, in the SrTiO₃ system, the most intense interactions will be obtained at short range. Following this procedure in a systematically way, it may be possible to determine the relevant parameters of our model and cast the irrelevant ones aside. The employed criteria to determine which electron-lattice terms will be implemented during the model construction is a set of cutoffs related with the electron-lattice coupling. All of them are explained below and shown in Fig. 4.6.

- δr_{pair} (Å): the two atoms whose relative displacement will be computed must be closer than cutoff-pair.
- δr_{ellat} (Å): the distance between the center of the Wannier functions and the position of the atoms must be smaller than the cutoff distance electron-lattice.
- $\delta \varepsilon_{\text{ellat}}$ (eV²): in order to avoid having an excess of variables in our model it is important to focus on the matrix elements of the training set $\{A^{\text{ellat}}\}$ which create more error. As result, this cutoff is selected comparing the following matrix elements. On the one hand, the matrix elements of the RAG geometry obtained from DFT calculations at short range ¹ and the electrostatics of the system, γ^{lr} , are considered. According to the model parametrization, these interactions can be also defined as interactions of the model without corrections. On the other hand, we take into account the interactions of the electron-lattice training set from DFT calculations. For a given calculation A^{ellat} in the training set, these terms are defined as $h_{ab}^{\text{DFT}}(A^{\text{ellat}})$. Employing γ_{ab}^{lr} , $h_{ab}^{\text{RAG,sr}}$ and $h_{ab}^{\text{DFT}}(A^{\text{ellat}})$ we can define the following quadratic difference

$$\left[h_{ab}^{\text{DFT}}(A^{\text{ellat}}) - (h_{ab}^{\text{RAG,sr}} + \gamma_{ab}^{\text{lr}}) \right]^2. \quad (4.26)$$

Now, we select an interaction group G and we sum through all the elements composing the group, all the unit cells in the super cell, and all the calculations of the electron-lattice training set,

$$\Theta_G^{\text{ellat}} = \sum_{A^{\text{ellat}}} \sum_{ab \in G} \left[h_{ab}^{\text{DFT}}(A^{\text{ellat}}) - (h_{ab}^{\text{RAG,sr}} + \gamma_{ab}^{\text{lr}}) \right]^2. \quad (4.27)$$

The interactions that will be taken into account are the ones integrated in the groups satisfying

$$\Theta_G^{\text{ellat}} > \delta \varepsilon_{\text{ellat}}. \quad (4.28)$$

The meaning of this cutoff will be better understood and detailed in further sections.

¹DFT calculations obtained from WANNIER-90 code can be splitted into short and large range term.

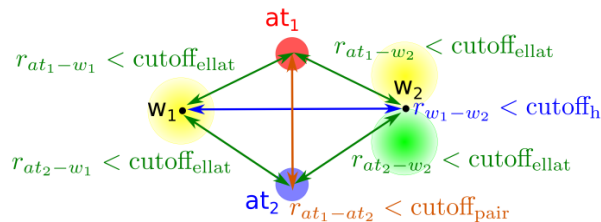


Figure 4.6. Cutoffs-ellat: δr_{ellat} (\AA), $\delta \epsilon_{\text{ellat}}$ (eV^2)
 Cutoff-pair: δr_{pair} (\AA)

4.3.4 Electron-electron Hamiltonian

Until now, we have built the band structure considering a Hamiltonian in the reference electron density (RED), neglecting the possible two-electron interactions linked to changes in Wannier functions occupations. In order to understand the RED concept and study the effects of occupation changes, we must to go back to the electronic density magnitude, $n(\vec{r})$ (it integrates to the number of electrons).

A. RED and deformation electron density

From second principles, the electronic density is treated as a perturbed quantity by splitting it into two parts. On the one hand, the *reference electron density* (RED), $n_0(\vec{r})$, is defined for each possible atomic configuration. Similar to perturbation theory, this value would correspond to a simple electron density to study, as close as possible to the real density, $n(\vec{r})$. In order to determine $n_0(\vec{r})$, for the sake of simplicity we consider a non-magnetic system. In particular, we will focus on an insulator or semiconductor compound. Under these assumptions the RED, $n_0(\vec{r})$, represents the ground state and it can be obtained from DFT calculations. Now, if we want to go beyond the ground state, a small *deformation charge density*, $\delta n(\vec{r})$, is taken, which would correspond to the perturbative term as follows,

$$n(\vec{r}) = n_0(\vec{r}) + \delta n(\vec{r}). \quad (4.29)$$

The electron density at a given point of the space can be expressed as a function of the Wannier orbitals of the basis set,

$$n(\vec{r}) = \sum_{\mathbf{ab}} d_{\mathbf{ab}} \chi_{\mathbf{a}}(\vec{r}) \chi_{\mathbf{b}}(\vec{r}) \quad (4.30)$$

where the element $d_{\mathbf{ab}}$ is defined as the *occupation matrix* of the Wannier functions $\chi_{\mathbf{a}}$ and $\chi_{\mathbf{b}}$. The RED can be computed similarly to $n(\vec{r})$,

$$n_0(\vec{r}) = \sum_{\mathbf{ab}} d_{\mathbf{ab}}^{(0)} \chi_{\mathbf{a}}(\vec{r}) \chi_{\mathbf{b}}(\vec{r}). \quad (4.31)$$

This deformation charge density might contain two-electron interactions:

- The charge doping by the addition of electrons to the bottom of the conduction band or by extracting electrons from the top of the valence band. This phenomenon is related with the simulation of *polarons*.
- The *excitation* of the electronic charge density in the neutral system by the transference of electrons from the valence to the conduction band. In this case, this effect is related to the excitons creation.
- For each one of the commented phenomenons, $\delta n(\vec{r})$ must capture the charge redistribution (response) of the remaining electrons to the induced change, *screening* phenomenon. It can

be viewed as resulting from an admixture of occupied and unoccupied states of the reference neutral configuration since the eigenstates represent a basis of the Hilbert space.

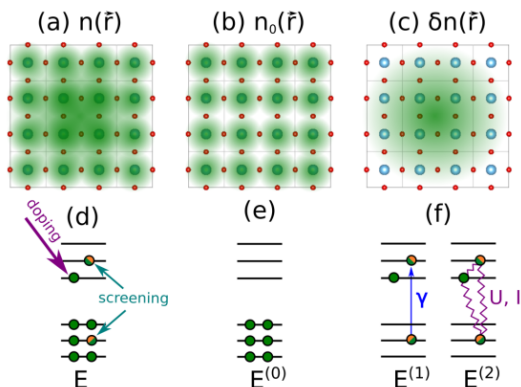


Figure 4.7. Schematic representation of the reference atomic structure and the reference and deformation electron densities. Illustrations (a)–(c) show the total density, the RAG and the deformation density for a semiconductor. Illustrations (d)–(f) exhibit the energy levels obtained for the neutral ground state. The occupation of a given state is determined by the full green circles. And the partial occupation is given by half filled orange/green circles. The notations $E^{(0)}$, $E^{(1)}$ and $E^{(2)}$ for the energies is related to the reference energy, one-electron contribution to the energy and two-electron contribution respectively [10].

(respectively, top of the valence band). Such a deformation density, captures both the doping and the system’s response to it, as previously exposed. The doping is represented by green balls in the electronic band diagrams while the screening is shown in orange.

In order to quantify the deformation density, we introduce a *deformation occupation matrix*, D_{ab} computed with the coefficients in Eq. 4.30 and Eq. 4.31

$$D_{ab} = d_{ab} - d_{ab}^{(0)}. \quad (4.32)$$

It can be defined in a similar way for each one of the spin channels s , D_{ab}^s . As result, the deformation density $\delta n(\vec{r})$ is given by

$$\delta n(\vec{r}, s) = \sum_{ab} D_{ab}^s \chi_a(\vec{r}) \chi_b(\vec{r}). \quad (4.33)$$

The total deformation charge, D_{ab} , can be expressed as the sum of the two spin components and is renamed by D_{ab}^U . The magnetization charge of the system, D_{ab}^I , is obtained as the difference between the two spin components,

$$D_{ab}^U = D_{ab}^\uparrow + D_{ab}^\downarrow \quad D_{ab}^I = D_{ab}^\uparrow - D_{ab}^\downarrow. \quad (4.34)$$

This last one only plays a role in spin-polarized system and is zero in a non-spin polarized compounds.

For better understanding of the RED and the deformation density concepts, an example is illustrated in Fig. 4.7, where the different densities are represented in the top cartoons and the associated electronic band occupations are outlined on the bottom. Here, the proposed splitting of the electronic density is applied on a doped semiconductor composed by two different types of atoms: large green/blue and small red balls in a 2D-square geometry and 3 atoms as motif. The RAG corresponds to the high-symmetry configuration in which the large atom is located at the center of the square, while the small atoms lie at the centers of the sides. The neutral system (undoped) is associated to the RED, Figs. 4.7(b), 4.7(e). Here, the system is in the ground state: the valence band is completely occupied while the conduction band is empty. At this moment, if some charge is added (or removed) Figs. 4.7(c), 4.7(f), the electronic cloud will be affected and will tend to screen the field caused by the extra charge. The doping electron (respectively, hole) will occupy the states at the bottom of the conduction band

B. *Electron-electron correction*

The electronic band structure changes depending on the occupation of the different states. At this moment, two-electron interactions must be included in Eq. (4.21) to go beyond the Born-Oppenheimer surface. These terms are embedded in deformation electronic density, as exciton phenomena involved in a wide variety of photovoltaic problems or alterations of the electronic density, as the addition of extra charge required to simulate polarons. In order to add the electron-electron coupling, an electron-electron correction term $\delta\gamma^{\text{el},s}$ is included in the building Hamiltonian to take into account the deformation electron density,

$$h_{\mathbf{ab}}^s = \gamma_{\mathbf{ab}}^{\text{RAG}} + \delta\gamma_{\mathbf{ab}}^{\text{ellat}} + \delta\gamma_{\mathbf{ab}}^{\text{el},s}. \quad (4.35)$$

 C. *Electron-electron terms*

According to Ref. [10], the electron-electron coupling is studied by the two-electron parameters U and I

$$\delta\gamma_{\mathbf{ab}}^{\text{el},s} = \sum_{\mathbf{a}'\mathbf{b}'} (D_{\mathbf{a}'\mathbf{b}'}^U U_{\mathbf{aba}'\mathbf{b}'} - D_{\mathbf{a}'\mathbf{b}'}^I I_{\mathbf{aba}'\mathbf{b}'}). \quad (4.36)$$

They are defined as four-center integrals. Considering $X = U, I$,

$$X_{\mathbf{aba}'\mathbf{b}'} = \int d^3r \chi_{\mathbf{a}'}(\vec{r}, s) \chi_{\mathbf{b}'}(\vec{r}, s) \int d^3r' \chi_{\mathbf{a}'}(\vec{r}', s) \chi_{\mathbf{b}'}(\vec{r}', s) g_X(\vec{r}, \vec{r}', s, s') \quad (4.37)$$

where g^U and g^I are the Hubbard and Stoner two-electron constants. The U and I terms match to the four-index integrals of Hartree-Fock theory. The Hubbard two-electron constant is computed as

$$g_U(\vec{r}, \vec{r}') = \frac{1}{|\vec{r} - \vec{r}'|} + \frac{1}{2} \left[\frac{\delta^2 E_{\text{xc}}}{\delta n(\vec{r}, \uparrow) \delta n(\vec{r}', \uparrow)} \Big|_{n_0} + \frac{\delta^2 E_{\text{xc}}}{\delta n(\vec{r}, \uparrow) \delta n(\vec{r}', \downarrow)} \Big|_{n_0} \right]. \quad (4.38)$$

It contains the classical electrostatic Hartree interaction (first term of the expression). This contribution is corrected by the second term where the elements $\delta^2 E_{\text{xc}} / \delta n(\vec{r}, s) \delta n(\vec{r}', s')$ captures the effective screening of the two-electron interactions due to exchange and correlation. It depends on the total deformation density described above, $D_{\mathbf{ab}'}^U$, and quantifies the energy needed to add or remove electrons.

The Stoner two-electron constant is related to the spin polarization and is given by the expression

$$g_I(\vec{r}, \vec{r}') = \frac{1}{2} \left[\frac{\delta^2 E_{\text{xc}}}{\delta n(\vec{r}, \uparrow) \delta n(\vec{r}', \downarrow)} \Big|_{n_0} - \frac{\delta^2 E_{\text{xc}}}{\delta n(\vec{r}, \uparrow) \delta n(\vec{r}', \uparrow)} \Big|_{n_0} \right]. \quad (4.39)$$

This magnitude considers the magnetic interactions providing the difference in interaction between electrons with parallel and antiparallel spins. Its origin is essentially quantum due to its exchange-correlation nature.

In the MODELMAKER language, $U_{\mathbf{aba}'\mathbf{b}'}$ and $I_{\mathbf{aba}'\mathbf{b}'}$ are electron-electron *terms* or *parameters* which modify a $h_{\mathbf{ab}}$ interaction. And a pair $\{U_{\mathbf{aba}'\mathbf{b}'}, I_{\mathbf{aba}'\mathbf{b}'}\}$ is an electron-electron *variable*.

D. Electron-electron training set

The dependence of the electron-electron correction with the perturbation of the occupations is studied by the simulation of first principle calculations for different density matrices D_{ab} . However, imposing occupations in DFT (constrained DFT) is difficult. As alternative, we can generate different configurations introducing a chemical potential in Wannier functions in order to change their population.

For the purpose of capturing electron-electron interactions, we run a set of first-principles configurations $\{A^{\text{el}}\}$ modifying the occupations in the Wannier orbitals. This perturbation is implemented introducing a chemical potential associated to a particular Wannier function c , μ_c , favouring its population/depopulation with charge. With frozen density, μ_c simply shifts the energy of χ_c in this way:

- $\mu_c < 0$: Wannier function χ_c reduces its energy favouring its population (Fig. 4.8(a)).
- $\mu_c > 0$: Wannier function χ_c increases its energy inclining toward the depopulation (Fig. 4.8(b)).

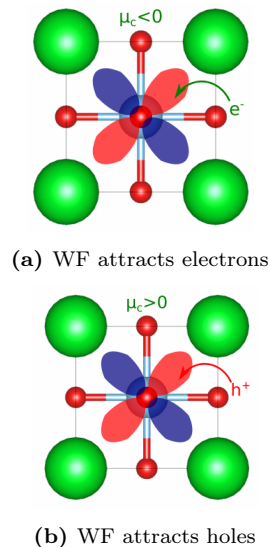


Figure 4.8. Changes in the chemical potential of Wannier functions (WF) favouring populated states or depopulated Wannier functions.

As result, it is possible to perturb the first-principle density matrix in a controlled way catching the electron-electron interactions by SCALE-UP code,

$$\tilde{h}_{ab}^{\text{SCF},\mu_{c,s}} = h_{ab}^{\text{SCF},\mu_{c,s}} - \mu_{c,s} \delta_{ac} \delta_{bc}. \quad (4.40)$$

As a simple example to understand the introduction of a chemical potential, Fig. 4.9 represents the energy levels for the H_2 molecule. On the left the system has not been perturbed. On the right, the chemical potential of the H_A atom has been increased. For both schemes the eigenfunctions are colored in blue. For the H_2 molecule without any perturbation, the coefficients of the eigenstates are equal. However, when we increase the chemical potential of H_A , χ_a favours its depopulation and χ_b tends to rise its occupation due to χ_a is higher in energy than χ_b . Thus, $c_A < c_B$.

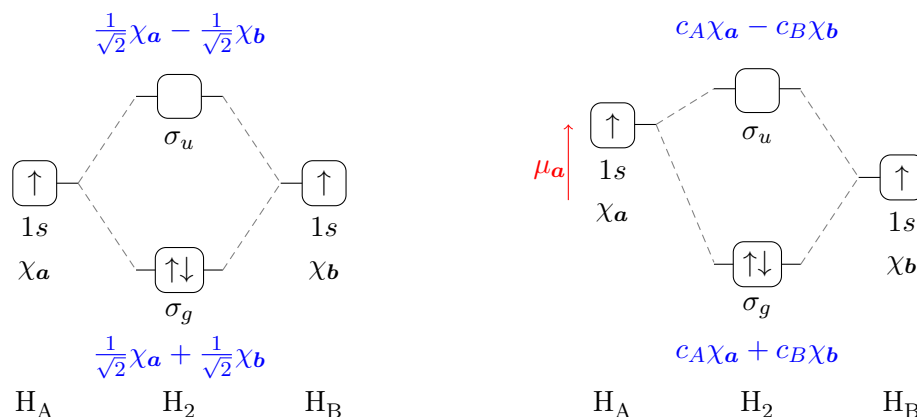


Figure 4.9. Molecular energy levels for the H_2 molecule. The rising of the chemical potential of the orbital χ_a favours the depopulation of the state while χ_b is populated. This fact is observed in the coefficients for the molecular states, where $c_A < c_B$.

E. *Electron-electron cutoff*

This section will be focused on the definition of the cutoffs for the electron-electron interactions. They are established between Wannier functions and are shown in Fig. 4.10.

- $\delta r_{\text{e}l\text{e}l}$ (Å): the distance between the center of two Wannier functions must be smaller than the cutoff distance electron-electron.
- $\delta \epsilon_{\text{e}l\text{e}l}$ (eV²): the energy cutoff for the electron-electron interactions is defined following the same reasoning as in the electron-lattice energy cutoff, $\delta \epsilon_{\text{e}l\text{a}t}$. In this case, the selected training set is the the related to the electron-electron coupling. Then, based on Eq. (4.41) and selecting the G group of interactions

$$\Theta_G^{\text{e}l\text{e}l} = \sum_{A^{\text{e}l\text{e}l}} \sum_{\mathbf{a}\mathbf{b} \in G} \left[h_{\mathbf{a}\mathbf{b}}^{\text{DFT}}(A^{\text{e}l\text{e}l}) - (h_{\mathbf{a}\mathbf{b}}^{\text{RAG,sr}} + \gamma_{\mathbf{a}\mathbf{b}}^{\text{lr}}) \right]^2. \quad (4.41)$$

The interactions that will be taken into account are the ones integrated in the groups satisfying

$$\Theta_G^{\text{e}l\text{e}l} > \delta \epsilon_{\text{e}l\text{e}l}. \quad (4.42)$$

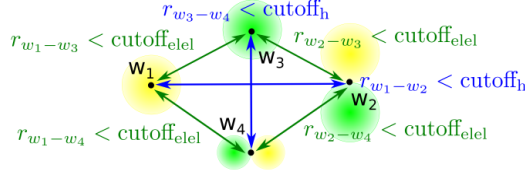


Figure 4.10. Cutoffs-elel: $\delta r_{\text{e}l\text{e}l}$ (Å), $\delta \epsilon_{\text{e}l\text{e}l}$ (eV²)

4.4 CALCULATION OF THE MODEL PARAMETERS

First of all, hereunder we summarize the concepts we are going to employ.

- Interaction : $h_{\mathbf{a}\mathbf{b}}$
- Parameters/Terms : $\vec{f}_{\mathbf{a}\mathbf{b},\lambda\nu}, \overleftrightarrow{g}_{\mathbf{a}\mathbf{b},\lambda\nu}, U_{\mathbf{a}\mathbf{b}\mathbf{a}'\mathbf{b}'}, I_{\mathbf{a}\mathbf{b}\mathbf{a}'\mathbf{b}'}$
- Variables : $\left\{ \vec{f}_{\mathbf{a}\mathbf{b},\lambda\nu}, \overleftrightarrow{g}_{\mathbf{a}\mathbf{b},\lambda\nu} \right\}, \left\{ U_{\mathbf{a}\mathbf{b}\mathbf{a}'\mathbf{b}'}, I_{\mathbf{a}\mathbf{b}\mathbf{a}'\mathbf{b}'} \right\}$

This section will be focused on the description of the procedure implemented on MODELMAKER script to compute the parameters of an electron-dynamical model. We exposed it in a similar way as Ref. [27]. The model must reproduce the training set calculations, characterized by geometry distortions or changes of the electronic occupations. In order to quantify the efficiency of the model when recreating the configurations in the training set $\{A\} = \{A^{\text{e}l\text{a}t}\} \cup \{A^{\text{e}l\text{e}l}\}$, it is defined a positive semi-definite function called *goal function* and represented by Θ . At this point, the developed methodology to perform the parameter fitting consists on the minimization of the goal function. In practice, the solution of such problems use to be a difficult task. The obtained equations to determine the free parameters (resulting from the goal function optimization) are typically nonlinear functions leading to multiminima solutions, which rises the computational cost. However, the expression of the built Hamiltonian in this work and the employed goal function (further shown) allow to find an analytic solution of the parameter calculations which in turn makes it feasible to identify the best model among the possible ones.

4.4.1 Definition of the goal function

In order to generate a model able to reproduce the training set calculations, the parameters, $\{p_i\}_{1 \leq i \leq P}$, will be computed fitting the model Hamiltonian interactions against first principles calculations. In line with this, we establish the expression for the goal function Θ measuring the difference between the following two elements.

◦ *First principles* (DFT) Hamiltonian matrix elements obtained for the different configurations of the training set $\{A\}$, $h_{ab}^{DFT}(A)$. These calculations leads to a set of first principles calculations for different *geometric* and *electronic* configurations. The entries h_{ab}^{DFT} of the first principles Hamiltonian matrix are calculated from DFT employing the WANNIER-90 code and represent the *interaction* between the two Wannier functions χ_a and χ_b .

◦ *Second-principles* Hamiltonian matrix elements calculated for the same set of configurations, $\{A\}$ and which depend on all parameters, $\{p_i\}$. In short, these elements represent the interactions of our model. They are labeled as $h_{ab}(A, \{p_i\})$.

Considering all these interactions for the super cell, the sum of their squares is computed. Finally, the global sum of all the calculations in the training set is performed and we obtain

$$\Theta(\{A\}, \{p_i\}) = \sum_A \sum_{ab} \left[h_{ab}^{DFT}(A) - h_{ab}^{\text{model}}(A, \{p_i\}) \right]^2. \quad (4.43)$$

4.4.2 Determining the variables: linear problem

According to the final Hamiltonian formulated for our model, it depends linearly with the parameters aimed to fit, $\{p_i\}$. So that, for each configuration we can write the Hamiltonian as

$$h(A) = \sum_i \theta_{Ai} p_i \quad (4.44)$$

where θ_{Ai} is a configuration-dependent constant that contains the correlation between the parameter x_i and DFT Hamiltonian element for a particular configuration A . The goal function can be then expressed in terms of the Eq. (4.44),

$$\Theta(\{A\}, \{p_i\}) = \sum_A \left[h(A)^{DFT} - \sum_i \theta_{Ai} p_i \right]^2. \quad (4.45)$$

Regarding the geometrical representation of Θ , it is a P -dimensional parabola which always satisfies $\Theta \geq 0$. Since the goal function is positive semi-definite, the eigenvalue of the associated Hessian will be always positive or zero. As result, a critical point of Θ must be a minimum.

The extrema of the goal function satisfy $\partial\Theta/\partial p_i = 0 \forall i$. Applying this equation for the P parameters, we obtain the linear system for the calculation of the $\{p_i\}$ parameters,

$$\sum_k A_{ik} p_k = b_i \quad \text{where} \quad \begin{aligned} A_{ik} &= \sum_A \theta_{iA} \theta_{kA} \\ b_i &= \sum_A \theta_{iA} h(A)^{DFT} \end{aligned} \quad (4.46)$$

However, there may be linear dependencies in our system of equations leading to a overdetermined model. Then we need to find which are the significant variables of our model. This problem is addressed in the following section.

4.4.3 Finding the best model of p variables

We consider \mathcal{X}_P as a set of P parameters which determine *all* the possible interactions in the system of interest. Now, we define a p -model as a model of p parameters: $\mathcal{X}_p \subset \mathcal{X}_P$. We need a procedure to built the best p -model, i.e., a criterion to choose the p parameters that minimizes the goal function. The first idea to solve this problem consists on computing all the possible combinations of p parameters of a set of P parameters and compare the resultant goal functions. However, this method is quite inefficient. For example, if we have a model with $P = 500$ parameters and we want to built a p -model such that $p = 20$, we have about 10^{35} different combinations of parameters, i.e., 10^{35} different models. As result, although we have selected an efficient strategy to calculate the parameters of a p -model, the analysis of so many combinations is unfeasible from the computational point of view.

In order to overcome this problem, the model search is restricted by a *step wise procedure with forward selection*. The method starts considering $p = 1$ and building all the P possible 1-model candidates with its respective goal functions. Let \mathcal{X}_1 represents of all the possible 1-models associated with a parameter set \mathcal{X} and $\Theta_1(p_i)$ the goal function considering only one parameter. The next step is focused on selecting the best 1-model by minimizing $\Theta_1(p_i)$ according to Sec. 4.4.2. Comparing the $\Theta_1(p_i) \forall i$, we choose the smallest one. At this point, we can identify the first parameter of our model, p_1^* which composes the set χ_1^* . Then, we move to $p + 1$ and we consider all the possible $(p + 1)$ -models which contains the variables of the best p -model, i.e, we study all the $p + 1$ -models with the constraint $\mathcal{X}_p^* \subset \mathcal{X}_{p+1}$. Keeping the p parameters of the best p -model, the $p + 1$ -models are built adding one by one the $P - p$ remaining variables. Again, we build the goal function $\Theta_p(\{\{p_j^*\}, p_i\}) \forall j \leq p, \forall p_i \neq p_j^*$ and it is minimized according to Sec. 4.4.2 and we select the p_i which makes minimum $\Theta_p(\{\{p_j^*\}, p_i\}) \forall j \leq p, \forall p_i \neq p_j^*$.

Below, the colored parameters in $p + 1$ -model come from the best p -model.

- Build best model 1 variable : $\{p_1^*\}$
- Build best model 2 variables : $\{p_1^*, p_2^*\}$
- Build best model 3 variables : $\{p_1^*, p_2^*, p_3^*\}$
- ...

Different parameters will be included in the model until obtain a goal function smaller than a fixed threshold.

4.5 STEPS IN THE MODEL GENERATION

This section will focus on the detailed description of the steps performed by the code once the interaction groups and the training have been generated. Here, the procedure described above for the construction of a model (Sec. 4.4) will be reproduced from a practical point of view, oriented to the development of a model for the STO system. Below, we explain the different steps.

4.5.1 Initial goal function

The *initial goal function* designed as Θ_o is computed according to the total goal function, Eq. (4.43) neglecting the Hamiltonian of the model. Clearly, we don't take into account the parameters of the model. In short,

$$\Theta_o(\{A\}, \{\emptyset\}) = \sum_A \sum_{ab} |h_{ab}^{\text{DFT}}(A)|^2. \quad (4.47)$$

This value can be computed as an accumulative function of the distance range of interaction of the Wannier orbitals and is measured in eV^2 . In other words, for each distance d , the result of Eq. (4.47) is computed considering all the interaction pairs \mathbf{a}, \mathbf{b} such that $|\vec{r}_{\mathbf{a}} - \vec{r}_{\mathbf{b}}| < d$,

$$\Theta_o(\{A\}, \{\emptyset\}, d) = \sum_A \sum_{\mathbf{ab} < d} |h_{\mathbf{ab}}^{\text{DFT}}(A)|^2. \quad (4.48)$$

Figure 4.11 plots the decimal logarithm of the initial goal functions as a function of the distance, shown with a continuous black curve. In addition, the Fig. 4.11 collects the decimal logarithm of the accumulative total number of Hamiltonian terms $h_{\mathbf{ab}}^{\text{DFT}}$ as a function of the distance, dotted red curve, of which those non-zero are displayed by the green curve.

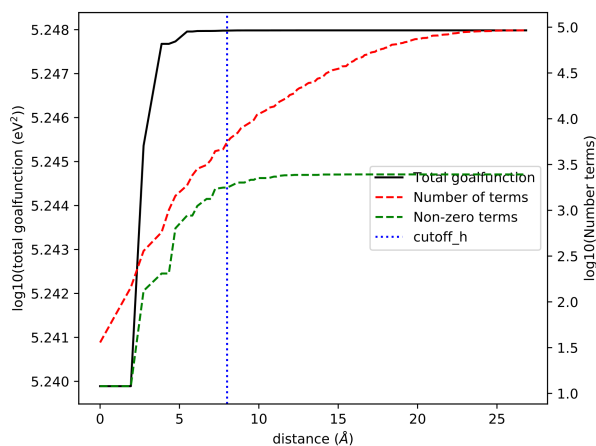


Figure 4.11. Representation of the decimal logarithm of the initial goal function, $\log(\Theta_o)$, as a function of the distance (black curve). Its values are determined by the left y -axis. On the right axis, the number of terms that would be included in the model for a given distance are plotted by the dotted red curve. Many of these terms are zero by symmetry. The number of non-zero terms are shown by the dotted green curve.

Attending to the shape of the curves, the analysis is divided in four regions. In support of this explanation, we shall employ Fig. 4.12. This picture illustrates a scheme of the SrTiO_3 system projected in the z -plane. By selecting the Ti atom of the home unit cell placed in the center of the drawing, we color different shells in the z -plane classifying the interactions according to the neighbours' distances (we neglect the Sr atom which does not present orbitals in the active set). We expect that the Hamiltonian matrix elements should decay fast with the distances between the Wanniers. This effect is represented in the figure by decreasing the intensity of the orange color with the distance.

◦ *Range 0-2 Å.* First region covers the interval from 0 Å to around 2 Å. Here, the initial goal function can be approximated as a plain with respect to the whole curve. This behaviour is due to the structure of SrTiO_3 crystal. In the RAG the lattice parameter is $a = 3.874$ Å [1] and the distance between two first neighbours is given by $a/2 = 1.973$ Å. Since Wannier orbitals are localized and centered in the respective atoms due to the rather ionic character of SrTiO_3 crystal, for distances smaller than $a/2$ there is no interaction among orbitals from two different atoms. At

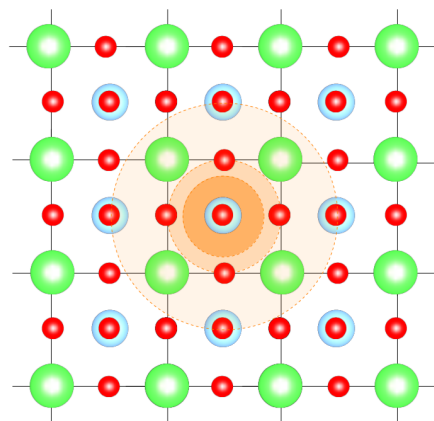


Figure 4.12. Different shells classifying interaction of the Wannier functions of Ti atom in the home unit cell with the Wannier functions of its neighbours. The more intense the orange color, the stronger the interaction between the orbitals.

that range of distances the only interactions which can be measured are the on-site ones, i.e., the present among the Wannier functions centered in the same atom. These interactions are shown in Fig. (4.12) by intense orange for the Ti atom in the home unit cell.

◦ *Range 2-4 Å*. Second region starts at 2 Å and extends until 4 Å. Here, we can see a sharp rise of the initial goal function. This abrupt is the consequence of the increasing of non-zero interactions, as is shown by the green dashed curve. Focusing on the Wannier functions we are studying, O $2p$ and Ti t_{2g} , the emerged interactions are the following:

- First shell of neighbours. Wannier functions in Ti - O atoms both at the home unit cell: distance $a/2 = 1.973$ Å.
- Second shell of neighbours. Wannier functions in O - O atoms both at the home unit cell : distance $a/\sqrt{2} = 2.739$ Å.
- Third shell of neighbours. Wannier functions in Ti - Ti $[\pm 1, 0, 0]$, Ti $[0, \pm 1, 0]$, Ti $[0, 0, \pm 1]$: distance $a = 3.874$ Å.
- Third shell of neighbours. Wannier functions in O - O $[\pm 1, 0, 0]$, O $[0, \pm 1, 0]$, O $[0, 0, \pm 1]$: distance $a = 3.874$ Å.

Summarizing, the Hamiltonian elements measuring first, second and third neighbour interactions are not zero in contrast to the first region. Even, its value is high due its proximity.

◦ *Range 4-8 Å*. In the interval from 4 Å to 8 Å, there exist small contributions to the initial goal function in spite of the number of non-zero terms continues growing. These behaviour is explained by the well localization of Wannier functions: at 4 Å Wannier functions interact, increasing the number of non-zero terms, but the value of the h_{ab}^{DFT} interactions is low due to small overlaps (Wannier functions decay exponentially).

◦ *Range > 8 Å*. Finally, working with distances larger than 8 Å the Hamiltonian elements are reduced to almost zero leading to a plain initial goal function.

According to the previous study, a reasonable value for the δr_h is $\delta r_h = 8.0$ Å. Employing this cutoff all the short range interactions are captured. In Fig. 4.11, this value is represented by the vertical dotted blue line.

4.5.2 Total goal function: model without parameters or electrostatics

At this stage, we are going to quantify the error of the model without considering the electrostatics of the interactions, γ_{ab}^{lr} , or the parameters $\{\vec{f}_{ab,\lambda\nu}, \overleftarrow{g}_{ab,\lambda\nu}, U_{ab}, I_{ab}\}$ (none of these contributions have, as yet, computed). In this way, h_{ab}^{model} is described by $\gamma_{ab}^{\text{RAG,sr}}$. Actually, the Hamiltonian of the model without parameters is just the first-principles calculation of the RAG,

$$\Theta(\{A\}, \{\emptyset\}) = \sum_A \sum_{ab} |h_{ab}^{\text{DFT}}(A) - h_{ab}^{\text{RAG}}|^2 = \sum_A \sum_{ab} |h_{ab}^{\text{DFT}}(A) - \gamma_{ab}^{\text{RAG,sr}}|^2. \quad (4.49)$$

4.5.3 Total goal function: model without parameters

For each one of the calculations in the training set, the unit cell and the super cell, the density matrices and the electrostatics are computed, $\delta\gamma_{ab}^{\text{lr}}$. Now, the total goal function is obtained considering for the Hamiltonian of the model the calculations at short range of the super cell (tight binding) and the electrostatics. Moreover, the value of δr_h truncates the sum of the model terms,

$$\begin{aligned}
 \Theta(\{A\}, \{\emptyset\}) &= \sum_A \left[\sum_{ab \leq \delta r_h} \left| h_{ab}^{\text{DFT}}(A) - h_{ab}^{\text{model}}(A, \{\emptyset\}) \right|^2 + \sum_{ab > \delta r_h} \left| h_{ab}^{\text{DFT}}(A) \right|^2 \right] = \quad (4.50) \\
 &= \sum_A \left[\sum_{ab \leq \delta r_h} \left| h_{ab}^{\text{DFT}}(A) - \left[\gamma_{ab}^{\text{RAG, sr}} + \gamma_{ab}^{\text{lg}}(A) \right] \right|^2 + \sum_{ab > \delta r_h} \left| h_{ab}^{\text{DFT}}(A) \right|^2 \right].
 \end{aligned}$$

The total goal function $\Theta(\{A\}, \{\emptyset\})$ can be splitted into two contributions: on the one hand, the error arising from the electron-lattice training set, Θ^{ellat} , and on the other hand, the error obtained from the calculations related to the electron-electron part, Θ^{elel} ,

$$\begin{aligned}
 \Theta^{\text{ellat}}(\{A^{\text{ellat}}\}, \{\emptyset\}) &= \sum_{A^{\text{ellat}}} \left[\sum_{ab \leq \delta r_h} \left| h_{ab}^{\text{DFT}}(A^{\text{ellat}}) - h_{ab}^{\text{model}}(A^{\text{ellat}}, \{\emptyset\}) \right|^2 + \sum_{ab > \delta r_h} \left| h_{ab}^{\text{DFT}}(A^{\text{ellat}}) \right|^2 \right] = \quad (4.51) \\
 &= \sum_{A^{\text{ellat}}} \left[\sum_{ab \leq \delta r_h} \left| h_{ab}^{\text{DFT}}(A^{\text{ellat}}) - \left[\gamma_{ab}^{\text{RAG, sr}} + \gamma_{ab}^{\text{lg}}(A^{\text{ellat}}) \right] \right|^2 + \sum_{ab > \delta r_h} \left| h_{ab}^{\text{DFT}}(A^{\text{ellat}}) \right|^2 \right]
 \end{aligned}$$

The same procedure is developed for electron-electron goal function, $\Theta_G^{\text{elel}}(\{A^{\text{elel}}\}, \{\emptyset\})$.

4.5.4 Groups contribution

In order to build an accurate model keeping computational efficiency, we select the interactions where the contribution to the error, i.e., to the total goal function, is higher. However, instead of studying each one of the interactions independently, the groups with larger error are taken into account. To determine which are these interaction groups, it is measured its individual error. Thus, the contribution of the G interaction group to the electron-lattice error without considering the model parameters, is computed as

$$\Theta^{\text{ellat}}(\{A^{\text{ellat}}\}, \{\emptyset\}) = \sum_{A^{\text{ellat}}} \left[\sum_{\substack{ab \leq \delta r_h, \\ ab \in G}} \left| h_{ab}^{\text{DFT}}(A^{\text{ellat}}) - \left[\gamma_{ab}^{\text{RAG, sr}} + \gamma_{ab}^{\text{lg}}(A^{\text{ellat}}) \right] \right|^2 + \sum_{\substack{ab > \delta r_h, \\ ab \in G}} \left| h_{ab}^{\text{DFT}}(A^{\text{ellat}}) \right|^2 \right] \quad (4.52)$$

The expression for the $\Theta_G^{\text{elel}}(\{A^{\text{elel}}\}, \{\emptyset\})$ is equivalent.

On the top of Fig. 4.13 the results for Θ_G^{ellat} are represented with blue lines. It is clear all the interactions in a group will be characterized by the same interactions distance. As consequence, it is possible to order the different groups regarding that distance. This order is shown in the x -axis, where the first groups are associated with short distance while the last ones will be characterized by large interaction distances. The red curve represents the accumulative sum of the errors, associated with the right y -axis. Its last value is the sum over all the groups, i.e., $\Theta^{\text{ellat}}(\{A^{\text{ellat}}\}, \{\emptyset\})$. On the bottom of the figure, the results for the electron-electron contributions are shown in a similar way.

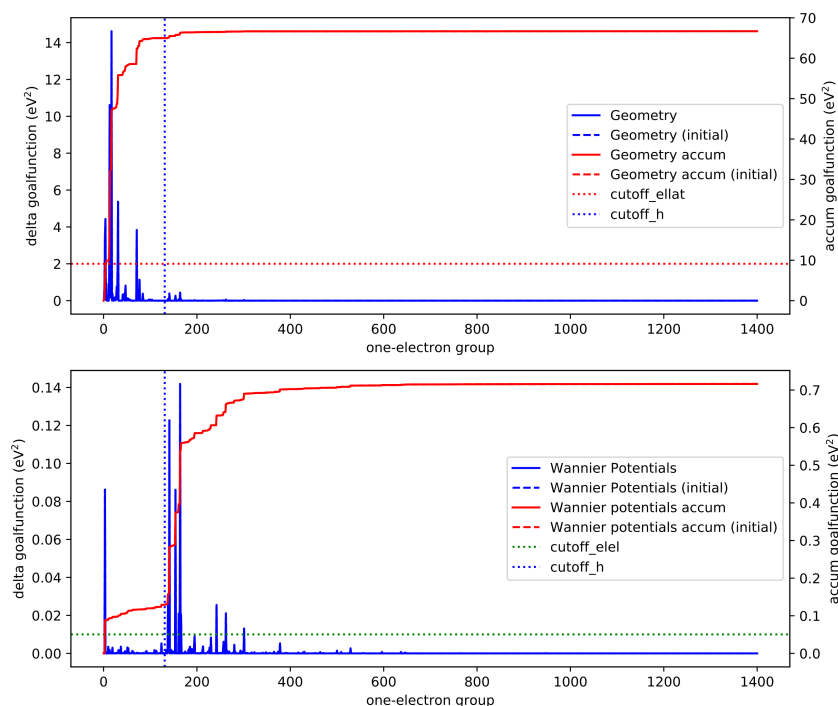


Figure 4.13. Electron-lattice (on the top) and electron-electron (on the bottom) error contributions to the total goal function without parameters for each one of the interaction groups ordered by distances (blue). The accumulative sum of these errors is represented by the red curve.

Now, it is possible to select the groups with the higher contribution to the total goal function according to the electron-lattice and electron-electron energy cutoffs (shown in the Fig. 4.13 by red and green horizontal lines respectively). In this sense, if

$$\Theta_G^{\text{ellat}} \left(\{A^{\text{ellat}}\}, \{\emptyset\} \right) > \delta\varepsilon_{\text{ellat}}, \quad (4.53)$$

the G interaction group is selected and electron-lattice variables will be generated for it. Similarly, if

$$\Theta_G^{\text{e1el}} \left(\{A^{\text{e1el}}\}, \{\emptyset\} \right) > \delta\varepsilon_{\text{e1el}} \quad (4.54)$$

electron-electron variables shall be computed for G . Here, we show the Tab. 4.2 with the different number of selected groups when varying the values of the energy cutoffs. On the top of the table, the rest of the cutoffs are shown, which remain fixed for all the constructed model.

	$\delta\varepsilon_{\text{ellat}}$ (eV ²)	$\delta\varepsilon_{\text{e1el}}$ (eV ²)	G_{ellat}	G_{e1el}
A	2.0	0.01	6	1
B	0.5	0.01	12	1
C	2.0	0.0025	6	5

Table 4.2. Selected groups for the variables generation for three different models where the energy cutoffs have been varied.

The number of picked groups increases when the energy cutoffs decrease.

4.5.5 Create electron variables

This procedure creates the electron variables to be fitted based on the choice of distance cutoffs δr_{pair} , δr_{ellat} , δr_{elel} . Each variables is associated to a unique group and a group can be related to several variables. Depending on the value of the cutoffs, the number of generated variables differs. This fact is exhibited in Tab. 4.3, where different models have been generated changing the mentioned distance cutoffs and keeping the rest fixed. These last ones are written down on the top of the table.

$\delta r_{\text{h}} = 8.0 \text{ \AA}$, $\delta \varepsilon_{\text{ellat}} = 2.0 \text{ eV}^2$, $\delta \varepsilon_{\text{elel}} = 0.01 \text{ eV}^2$					
	$\delta r_{\text{pair}} \text{ (\AA)}$	$\delta r_{\text{ellat}} \text{ (\AA)}$	$\delta r_{\text{elel}} \text{ (\AA)}$	#Variables _{ellat}	#Variables _{elel}
A	2.5	4.00	0.01	14	2
D	4.00	4.00	0.01	65	2
E	2.5	6.00	0.01	45	2

Table 4.3. Number of generated variables for three different models where the distance cutoffs have been changed.

The number of variables grows with the increase in distance cutoffs.

4.5.6 Fitting electron terms

This procedure is employed to find the optimal model obtained from the fit of the electron variables against the training set (Sec. 4.4.3). Fig. 4.14 represents the final goal function versus the number of variables (pair of parameters) in the model. The dots correspond to electron-lattice variables while the crosses are related to electron-electron variables.

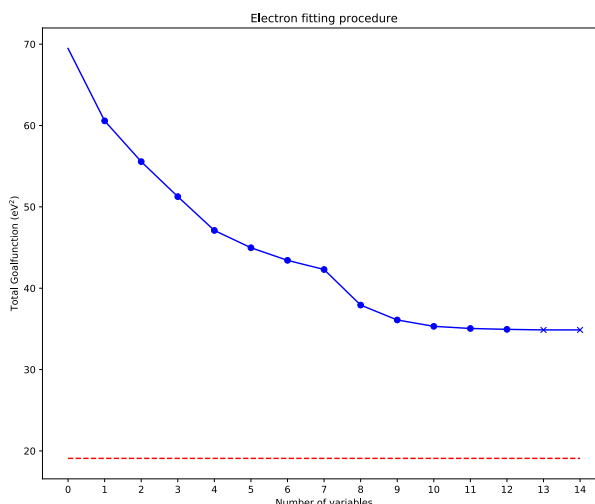


Figure 4.14. Blue line represents the obtained final total goal function versus the number of variables considered in the model.

In the figure we can see how the total goal function decreases when the number of included variables is higher.

RESULTS

At this point, we are going to validate the accuracy of our proposed strategy. In order to check the method, we will discuss its application to different configurations of the SrTiO_3 system out of the training set. Moreover, for the purpose of building the best model regarding a balance between accuracy and efficiency, we explore different values for the cutoff variables. Here, the validation of the models is based on the comparison of the band diagram representations obtained from first principles calculations versus second principles calculations. The latter take advantage of the models. The first principles bands data have been obtained from calculations with the SIESTA code based on density-functional theory by local density approximation (LDA). In the representation, they are shown in blue while the band diagrams from second principles calculations are colored in red. Let us now discuss the predictions for the electronic band structure that our obtained models yield for SrTiO_3 's ferroelectric and antiferrodistortive phases.

5.1 FERROELECTRIC PHASE IN SrTiO_3

In its pure, unstressed form, SrTiO_3 is an incipient ferroelectric. It remains paraelectric for high temperatures. However, chemical or isotopic substitution, as well as the inducement of stress, easily disturb this sensitive state, resulting in ferroelectricity. According to the latter effect, here we apply an epitaxial compressive strain on the cubic paraelectric phase of SrTiO_3 . This strain is applied on the XY -plane arising an elongation in the z -axis. As result, the polarization in z -axis is induced and the ferroelectric phase emerges.

In Fig. 5.2 we compare the full first-principles bands for a SrTiO_3 unit cell in a ferroelectric phase with those obtained by second principles from models corresponding to different values of δr_h , keeping the rest cutoffs.

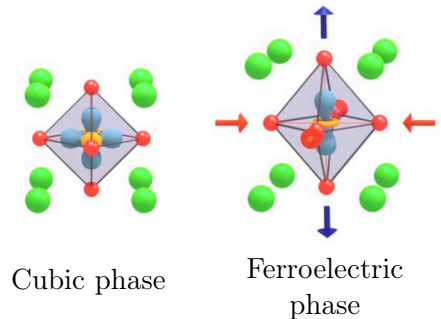


Figure 5.1. Phase transition from cubic paraelectric structure to a tetragonal ferroelectric phase when it is applied an epitaxial compressive strain in the plane. [16]

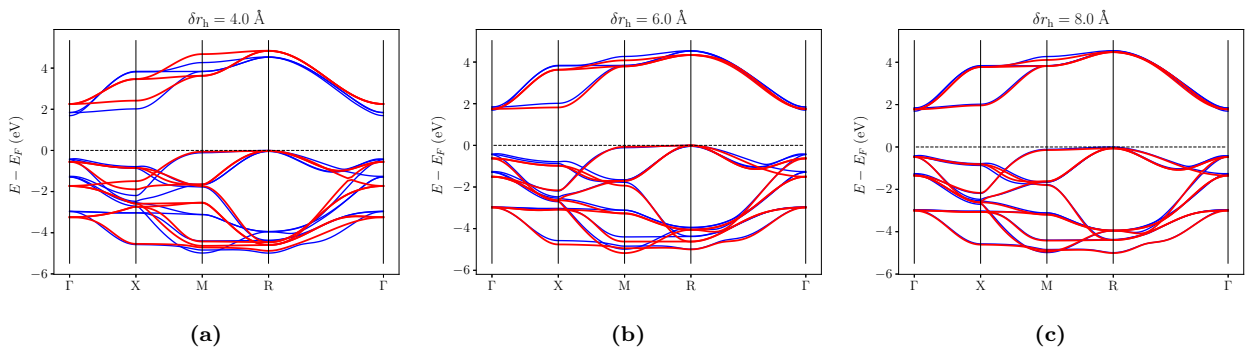


Figure 5.2. Representation of the bands of ferroelectric SrTiO_3 for various values of δr_h . Blue lines show the bands obtained from first principles and the red ones, the results from the second principles models.

According to the obtained representations, we extract two conclusions. Firstly, choosing a suitable cutoff δr_h is an important task to develop a descriptive model of SrTiO₃ system. Secondly the matching between red and blue curves fits better with the increment of δr_h . Thus, we can reproduce the bands for a realistic system out of the training set.

5.2 ANTIFERRODISTORTIVE PHASE IN SrTiO₃

SrTiO₃ undergoes one phase transition from a paraelectric cubic phase to a non-polar antiferrodistortive (AFD) tetragonal phase (I4/mcm, No 140) at a temperature $T_C \approx 105$ K. This AFD phase arises from rotations of oxygen octahedra around the tetragonal axis, such that the total atomic displacements keep the crystal non-polar (see Fig. 5.3). The ground state is characterized by antiphase rotations. The rotations are accompanied by a small deformation of the unit cell that becomes tetragonal. The driving force which produces the octahedra rotation in perovskites is the optimization of the Oxygen anions coordination environment of underbonded Sr-site cations.

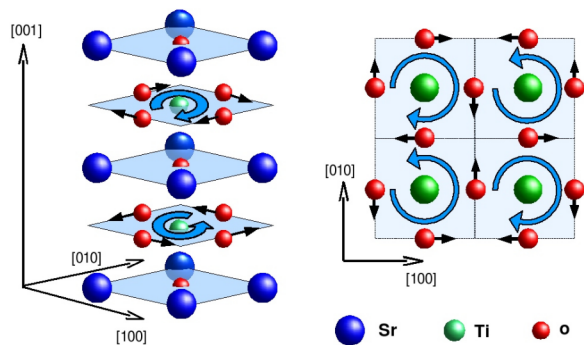


Figure 5.3. Schematic representation of the oxygen pattern of displacements in the low temperature tetragonal bulk SrTiO₃, corresponding to AFD distortions. At left is reported a view allowing to see the out-of-phase rotation of each successive oxygen plane along the $[0, 0, 1]$ direction. At right is reported a projection on the TiO₂ atomic plane. Reprinted with permission from E. Bousquet’s Ph.D. thesis, Ref. [4].

Electronic band structure of a SrTiO₃ antiferrodistortive geometry is obtained from first principles and second principles calculations. The employed reference geometry for this phase is a supercell $2 \times 2 \times 2$ since the antiphase rotation of the octahedra can’t be reproduced by translations of the unit cell. For this geometry, different models have been built with $\delta r_h = 8.0 \text{ \AA}$ and changing the cutoff variables related to the electron-lattice coupling: $\delta r_{\text{pair}}, \delta r_{\text{ellat}}, \delta \varepsilon_{\text{ellat}}$. On the one hand, the value of $\delta r_h = 8.0 \text{ \AA}$ has been selected according to Fig. 4.2. There, we already compared four models varying the this cutoff and keeping fixed the remainder. The calculations were made for the unit cell of the SrTiO₃ cubic phase. We found the second principles bands matched quite well with first principles calculations when employing $\delta r_h = 8.0 \text{ \AA}$. Here, this model will be denoted as *reference model* and its associated electronic band structure from first and second principles is shown in Fig 5.4(a). On the other hand, the values of the electron-lattice cutoffs have been modified regarding the reference model. In other words, we have built three additional models by modifying the electron-lattice cutoff variables one by one, keeping the rest fixed. The electronic band structures of these models are shown in Figs. 5.4(c), 5.4(b) and 5.4(d).

At first, in Fig. 5.4, we represent the results for the reference model. Secondly, the Fig. 5.4(b) employs a model where $\delta \varepsilon_{\text{ellat}}$ has been lowered. The reduction of this cutoff introduces more interaction groups in the model which contribute to diminish the error of the electron-lattice correction. Thirdly, in Fig. 5.4(c) δr_{ellat} has been increased with respect the reference model. This allows the inclusion of atom-Wannier pairs that are farther apart (see Fig. 4.6). Finally, for the fourth band diagram, Fig. 5.4(d), the improved cutoff has been δr_{pair} . Here, atom-atom pairs farther apart are taken into account.

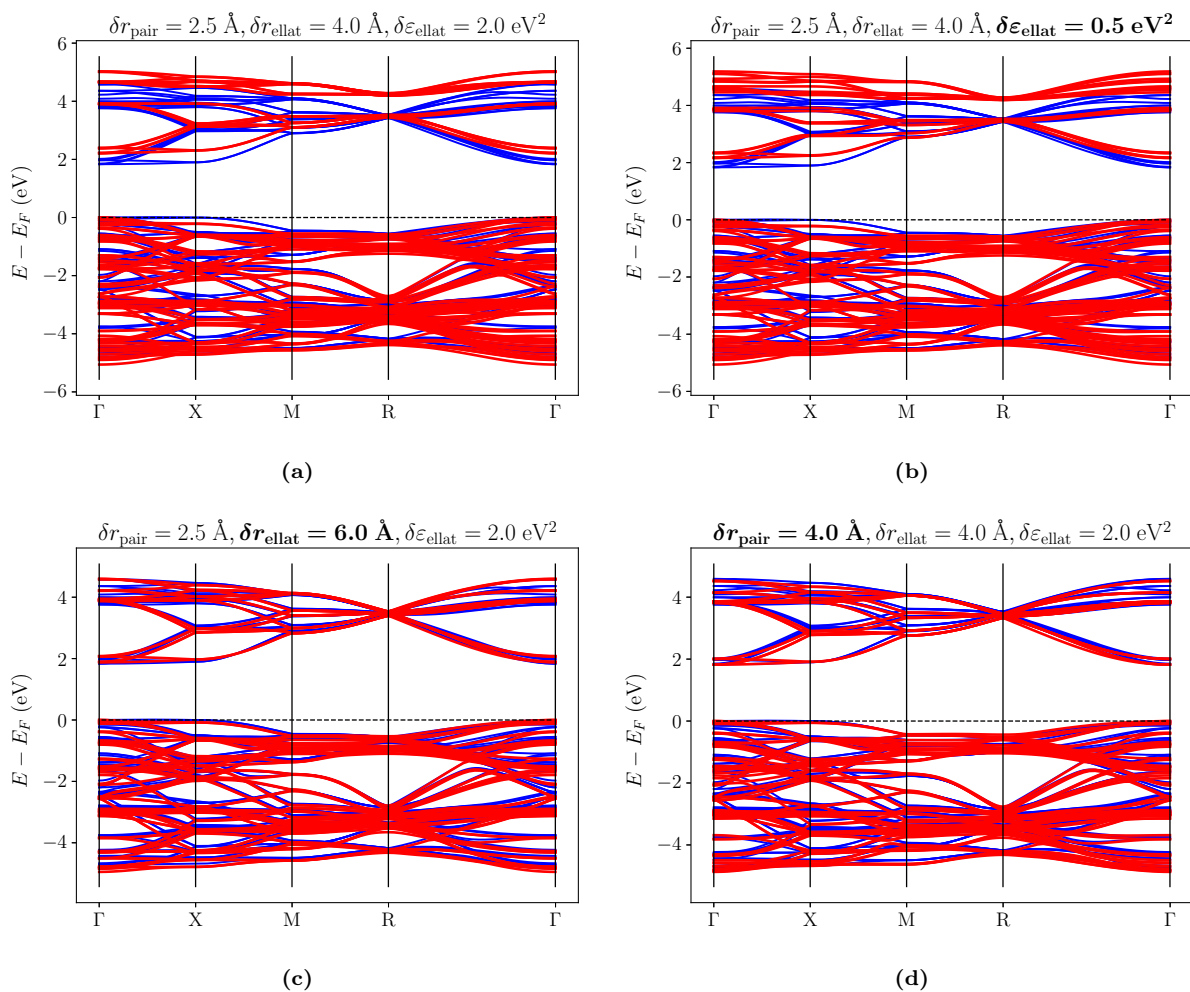


Figure 5.4. Representation of the bands of antiferrodistortive SrTiO₃ for different values of the electron-lattice cutoffs. Blue lines represent the bands obtained from first principles, while the results from the second-principles model are shown in red. On top of each plot we indicate the corresponding values of the cutoffs.

Analysing the different electronic band structure, we observe neither the reference model nor the model improving $\delta\epsilon_{\text{ellat}}$ are able to reproduce the band diagram of this geometry. The main and obvious discrepancies with the first principles calculations are the band gap and the energies obtained for the conduction band in the R symmetry point. On the one hand, the band gap from second principles is larger than the one obtained from first principles. This fact shifts the conduction band with respect to the blue bands. On the other hand, from first principles calculations the energies at R point are degenerated for the conduction band. Looking at second principles calculations, this degeneration is splitted into two energies. Now, attending to models where the distance cutoffs δr_{ellat} and δr_{pair} have been increased, we observe a clear improvement of the matching between red and blue bands. In such cases, the band gap and the degeneration of the R point in the conduction band are perfectly reproduced. The large amount of bands in the valence band makes it difficult to compare the results for the two calculations however we can see a good agreement at a glance. By analyzing the conduction band, we can see how the bands from the different calculations fit quite well. As consequence, the cutoffs δr_{ellat} and δr_{pair} play a decisive role in the construction of the SrTiO₃ model. Since when these cutoffs are increased, the model includes more variables related to the distortions in the lattice, very important in the rotations of the octahedra.

CONCLUSIONS

In this work we have first explained the negative compressibility in $\text{LaAlO}_3/\text{SrTiO}_3$ interfaces. Secondly, we have proposed a mechanism to understand this untypical phenomenon based on the polaron formation in low density regime. Due to the challenge of simulating polarons from first principles, we have described a second-principles approach that reduces the computational cost of such simulations. Finally, we have checked our method in different SrTiO_3 geometry structures. From this work, we can emphasize the following results.

- It has been checked the computational efficiency of second principles versus first principles calculation keeping the accuracy. In Tab. 6.1 the computational times for the calculation of the electronic band structure from SIESTA (first principles based code) and SCALE-UP are collected. The advantage of second principles is clear.

	Timing SIESTA	Timing SCALE-UP
Ferroelectric phase	2' 38"	0' 7"
Antiferrodistortive phase	46' 29"	4' 39"

Table 6.1. Wall times obtained in the calculation of electronic band structures of ferroelectric and antiferrodistortive phases of SrTiO_3 from first (SIESTA code) and second principles (SCALE-UP software).

- We have performed second-principles simulations on complex systems with efficient and asymptotically convergent DFT methods. Despite having parametrized the Hamiltonian of these systems, it is possible to improve the approximation systematically by adjusting the cutoff variables.
- In order to study the accuracy of our method, it has been validated on a functional oxide such as the SrTiO_3 system.
- Although the different models have been built fitting the parameters according to the generated training set, we have obtained the model that reproduces the electronic band structure in further systems for which the SrTiO_3 has been fitted, as a ferroelectric phase or antiferrodistortive SrTiO_3 system.
- After verifying that our method is able to reproduce SrTiO_3 systems in an efficient and accuracy way, this work concludes the first step in solving simulations in SrTiO_3 polarons. In future works, we shall develop lattice models and we combine both electron models (studied in this work) and lattice models to simulate the creation of polaron.

BIBLIOGRAPHY

- [1] P. Aguado-Puente, P. Garcia-Fernandez, and J. Junquera. Interplay of couplings between antiferrodistortive, ferroelectric, and strain degrees of freedom in monodomain $\text{PbTiO}_3/\text{SrTiO}_3$ superlattices. *Physical review letters*, 107(21):217601, 2011.
- [2] G. Allison, E. A. Galaktionov, A. K. Savchenko, S. S. Safonov, M. M. Fogler, M. Y. Simmons, and D. A. Ritchie. Thermodynamic density of states of two-dimensional gas systems near the apparent metal-insulator transition. *Phys. Rev. Lett.*, 96:216407, 2006.
- [3] M. T. Bohr, R. S. Chau, T. Ghani, and K. Mistry. The high-k solution. *IEEE spectrum*, 44(10):29–35, 2007.
- [4] E. Bousquet. *First-Principles study of ferroelectric oxidenanostructures*. Université de Liège, Ph. d. thesis, 2008.
- [5] E. Breckenfeld, Richard Wilson, and L. Martin. Effect of growth induced (non)stoichiometry on the thermal conductivity, permittivity, and dielectric loss of LaAlO_3 films. *Applied Physics Letters*, 103, 2013.
- [6] C. Cen, S. Thiel, J. Mannhart, and J. Levy. Oxide nanoelectronics on demand. *Science*, 323(5917):1026–1030, 2009.
- [7] Y. J. Chang, A. Bostwick, Y. S. Kim, K. Horn, and E. Rotenberg. Structure and correlation effects in semiconducting SrTiO_3 . *Phys. Rev. B*, 81:235109, 2010.
- [8] A. S. Alexandrov (editor). *Polarons in Advanced Materials*. Springer, Dordrecht, 2007.
- [9] P. García-Fernández, P. Aguado-Puente, and J. Junquera. Lattice screening of the polar catastrophe and hidden in-plane polarization in $\text{KbO}_3/\text{BaTiO}_3$ interfaces. *Physical Review B*, 87(8):085305, 2013.
- [10] P. García-Fernández, J. C. Wojdeł, J. Íñiguez, and J. Junquera. Second-principles method for materials simulations including electron and lattice degrees of freedom. *Phys. Rev. B*, 93:195137, 2016.
- [11] J. Junquera, P. García-Fernández, and M. Stengel. Mechanisms to enhance the capacitance beyond the classical limits in capacitors with free-electron-like electrodes. *Phys. Rev. B*, 99:235127, 2019.
- [12] I. Kawayama, K. Kotani, M. Misra, H. Murakami, and M. Tonouchi. Dielectric properties of $(\text{Ba,Sr})\text{TiO}_3$ thin films in mhz and thz frequency regions: Quantitative evaluation of the orientational polarization. *Japanese Journal of Applied Physics*, 53:09PD06, 2014.
- [13] T. Kopp and J. Mannhart. Calculation of the capacitances of conductors: Perspectives for the optimization of electronic devices. *Journal of Applied Physics*, 106(6):064504, 2009.

-
- [14] L. Li, C. Richter, S. Paetel, T. Kopp, J. Mannhart, and R. C. Ashoori. Very large capacitance enhancement in a two-dimensional electron system. *Science*, 332(6031):825–828, 2011.
- [15] L. Li, C Richter, S Paetel, T Kopp, J Mannhart, and RC Ashoori. Large capacitance enhancement and negative compressibility of two-dimensional electronic systems at laalo $\sqrt{3}$ /sratio $\sqrt{3}$ interfaces. *arXiv preprint arXiv:1006.2847*, 2010.
- [16] Z. Liao and J. Zhang. Metal-to-insulator transition in ultrathin manganite heterostructures. *Applied Sciences*, 9(1):144, 2019.
- [17] J. Mannhart and D. G. Schlom. Oxide interfaces—an opportunity for electronics. *Science*, 327(5973):1607–1611, 2010.
- [18] N. Marzari, A. A. Mostofi, J. R. Yates, I. Souza, and D. Vanderbilt. Maximally localized wannier functions: Theory and applications. *Rev. Mod. Phys.*, 84:1419–1475, 2012.
- [19] N. Marzari, D. Vanderbilt, and M. C. Payne. Ensemble density-functional theory for ab initio molecular dynamics of metals and finite-temperature insulators. *Phys. Rev. Lett.*, 79:1337–1340, 1997.
- [20] P. González Mazón. *First-order correction of current quantum capacitor models*. Universidad de Cantabria, Trabajo de Fin de Grado, 2019.
- [21] N. Nakagawa, H. Y. Hwang, and D. A. Muller. Why some interfaces cannot be sharp. *Nature materials*, 5(3):204–209, 2006.
- [22] A. Ohtomo and H.Y. Hwang. A high-mobility electron gas at the laalo $\sqrt{3}$ /sratio $\sqrt{3}$ heterointerface. *Nature*, 427(6973):423–426, 2004.
- [23] M. Stengel, P. Aguado-Puente, N. A. Spaldin, and J. Junquera. Band alignment at metal/ferroelectric interfaces: Insights and artifacts from first principles. *Phys. Rev. B*, 83:235112, 2011.
- [24] K. Van Benthem, C. Elsässer, and R.H. French. Bulk electronic structure of sratio $\sqrt{3}$: Experiment and theory. *Journal of applied physics*, 90(12):6156–6164, 2001.
- [25] D. Vanderbilt. *Berry Phases in Electronic Structure Theory: Electric Polarization, Orbital Magnetization and Topological Insulators*. Cambridge University Press, 2018.
- [26] G. D. Wilk, R. M. Wallace, and JáM Anthony. High- κ gate dielectrics: Current status and materials properties considerations. *Journal of applied physics*, 89(10):5243–5275, 2001.
- [27] J. C. Wojdeł, P. Hermet, M. P. Ljungberg, P. Ghosez, and J. Íñiguez. First-principles model potentials for lattice-dynamical studies: general methodology and example of application to ferroic perovskite oxides. *Journal of Physics: Condensed Matter*, 25(30):305401, 2013.
- [28] P. Zubko, S. Gariglio, M. Gabay, P. Ghosez, and J.M. Triscone. Annual review of condensed matter physics, vol. 2. 2011.

Appendix

The permissions for the different figures extracted from the bibliography are included below.

SPRINGER NATURE LICENSE TERMS AND CONDITIONS

Jun 06, 2021

This Agreement between University -- Nayara Carral ("You") and Springer Nature ("Springer Nature") consists of your license details and the terms and conditions provided by Springer Nature and Copyright Clearance Center.

License Number	5083181225247
License date	Jun 06, 2021
Licensed Content Publisher	Springer Nature
Licensed Content Publication	Nature Materials
Licensed Content Title	Why some interfaces cannot be sharp
Licensed Content Author	Naoyuki Nakagawa et al
Licensed Content Date	Jan 22, 2006
Type of Use	Thesis/Dissertation
Requestor type	academic/university or research institute
Format	electronic
Portion	figures/tables/illustrations
Number of figures/tables /illustrations	1
High-res required	no

Will you be translating?	no
Circulation/distribution	1 - 29
Author of this Springer Nature content	no
Title	Enhancement of negative compressibility in two-dimensional electron gases at oxide interfaces.
Institution name	University of Cantabria
Expected presentation date	Jul 2021
Portions	Figure 1
Requestor Location	University Santander
Total	Santander, 39005 Spain Attn: University
Terms and Conditions	0.00 USD

Springer Nature Customer Service Centre GmbH Terms and Conditions

This agreement sets out the terms and conditions of the licence (the **Licence**) between you and **Springer Nature Customer Service Centre GmbH** (the **Licensor**). By clicking 'accept' and completing the transaction for the material (**Licensed Material**), you also confirm your acceptance of these terms and conditions.

1. Grant of License

1. 1. The Licensor grants you a personal, non-exclusive, non-transferable, world-wide licence to reproduce the Licensed Material for the purpose specified in your order only. Licences are granted for the specific use requested in the order and for no other use, subject to the conditions below.

1. 2. The Licensor warrants that it has, to the best of its knowledge, the rights to license reuse of the Licensed Material. However, you should ensure that the material you are requesting is original to the Licensor and does not carry the copyright of another entity (as credited in the published version).

1. 3. If the credit line on any part of the material you have requested indicates that it was reprinted or adapted with permission from another source, then you should also seek permission from that source to reuse the material.

2. Scope of Licence

2. 1. You may only use the Licensed Content in the manner and to the extent permitted by these Ts&Cs and any applicable laws.

2. 2. A separate licence may be required for any additional use of the Licensed Material, e.g. where a licence has been purchased for print only use, separate permission must be obtained for electronic re-use. Similarly, a licence is only valid in the language selected and does not apply for editions in other languages unless additional translation rights have been granted separately in the licence. Any content owned by third parties are expressly excluded from the licence.

2. 3. Similarly, rights for additional components such as custom editions and derivatives require additional permission and may be subject to an additional fee. Please apply to Journalpermissions@springernature.com/bookpermissions@springernature.com for these rights.

2. 4. Where permission has been granted **free of charge** for material in print, permission may also be granted for any electronic version of that work, provided that the material is incidental to your work as a whole and that the electronic version is essentially equivalent to, or substitutes for, the print version.

2. 5. An alternative scope of licence may apply to signatories of the [STM Permissions Guidelines](#), as amended from time to time.

3. Duration of Licence

3. 1. A licence for is valid from the date of purchase ('Licence Date') at the end of the relevant period in the below table:

Scope of Licence	Duration of Licence
Post on a website	12 months
Presentations	12 months
Books and journals	Lifetime of the edition in the language purchased

4. Acknowledgement

4. 1. The Licensor's permission must be acknowledged next to the Licenced

Material in print. In electronic form, this acknowledgement must be visible at the same time as the figures/tables/illustrations or abstract, and must be hyperlinked to the journal/book's homepage. Our required acknowledgement format is in the Appendix below.

5. Restrictions on use

5. 1. Use of the Licensed Material may be permitted for incidental promotional use and minor editing privileges e.g. minor adaptations of single figures, changes of format, colour and/or style where the adaptation is credited as set out in Appendix 1 below. Any other changes including but not limited to, cropping, adapting, omitting material that affect the meaning, intention or moral rights of the author are strictly prohibited.

5. 2. You must not use any Licensed Material as part of any design or trademark.

5. 3. Licensed Material may be used in Open Access Publications (OAP) before publication by Springer Nature, but any Licensed Material must be removed from OAP sites prior to final publication.

6. Ownership of Rights

6. 1. Licensed Material remains the property of either Licensor or the relevant third party and any rights not explicitly granted herein are expressly reserved.

7. Warranty

IN NO EVENT SHALL LICENSOR BE LIABLE TO YOU OR ANY OTHER PARTY OR ANY OTHER PERSON OR FOR ANY SPECIAL, CONSEQUENTIAL, INCIDENTAL OR INDIRECT DAMAGES, HOWEVER CAUSED, ARISING OUT OF OR IN CONNECTION WITH THE DOWNLOADING, VIEWING OR USE OF THE MATERIALS REGARDLESS OF THE FORM OF ACTION, WHETHER FOR BREACH OF CONTRACT, BREACH OF WARRANTY, TORT, NEGLIGENCE, INFRINGEMENT OR OTHERWISE (INCLUDING, WITHOUT LIMITATION, DAMAGES BASED ON LOSS OF PROFITS, DATA, FILES, USE, BUSINESS OPPORTUNITY OR CLAIMS OF THIRD PARTIES), AND WHETHER OR NOT THE PARTY HAS BEEN ADVISED OF THE POSSIBILITY OF SUCH DAMAGES. THIS LIMITATION SHALL APPLY NOTWITHSTANDING ANY FAILURE OF ESSENTIAL PURPOSE OF ANY LIMITED REMEDY PROVIDED HEREIN.

8. Limitations

8. 1. *BOOKS ONLY:* Where '**reuse in a dissertation/thesis**' has been selected the following terms apply: Print rights of the final author's accepted manuscript (for clarity, NOT the published version) for up to 100 copies, electronic rights for

use only on a personal website or institutional repository as defined by the Sherpa guideline (www.sherpa.ac.uk/romeo/).

8. 2. For content reuse requests that qualify for permission under the [STM Permissions Guidelines](#), which may be updated from time to time, the STM Permissions Guidelines supersede the terms and conditions contained in this licence.

9. Termination and Cancellation

9. 1. Licences will expire after the period shown in Clause 3 (above).

9. 2. Licensee reserves the right to terminate the Licence in the event that payment is not received in full or if there has been a breach of this agreement by you.

Appendix 1 – Acknowledgements:

For Journal Content:

Reprinted by permission from [**the Licensor**]: [**Journal Publisher** (e.g. Nature/Springer/Palgrave)] [**JOURNAL NAME**] [**REFERENCE CITATION** (Article name, Author(s) Name), [**COPYRIGHT**] (year of publication)]

For Advance Online Publication papers:

Reprinted by permission from [**the Licensor**]: [**Journal Publisher** (e.g. Nature/Springer/Palgrave)] [**JOURNAL NAME**] [**REFERENCE CITATION** (Article name, Author(s) Name), [**COPYRIGHT**] (year of publication), advance online publication, day month year (doi: 10.1038/sj.[**JOURNAL ACRONYM**].)]

For Adaptations/Translations:

Adapted/Translated by permission from [**the Licensor**]: [**Journal Publisher** (e.g. Nature/Springer/Palgrave)] [**JOURNAL NAME**] [**REFERENCE CITATION** (Article name, Author(s) Name), [**COPYRIGHT**] (year of publication)]

Note: For any republication from the British Journal of Cancer, the following credit line style applies:

Reprinted/adapted/translated by permission from [**the Licensor**]: on behalf of Cancer Research UK: : [**Journal Publisher** (e.g. Nature/Springer/Palgrave)] [**JOURNAL NAME**] [**REFERENCE CITATION** (Article name, Author(s) Name), [**COPYRIGHT**] (year of publication)]

For Advance Online Publication papers:

Reprinted by permission from The [**the Licensor**]: on behalf of Cancer Research UK: [**Journal Publisher** (e.g. Nature/Springer/Palgrave)] [**JOURNAL NAME**] [**REFERENCE CITATION** (Article name, Author(s) Name), [**COPYRIGHT**] (year of publication), advance online publication, day month year (doi: 10.1038/sj.[**JOURNAL ACRONYM**].)]

For Book content:

Reprinted/adapted by permission from **[the Licensor]**: **[Book Publisher** (e.g. Palgrave Macmillan, Springer etc) **[Book Title]** by **[Book author(s)]**
[COPYRIGHT] (year of publication)

Other Conditions:

Version 1.3

Questions? customercare@copyright.com or +1-855-239-3415 (toll free in the US) or +1-978-646-2777.

THE AMERICAN ASSOCIATION FOR THE ADVANCEMENT OF
SCIENCE LICENSE
TERMS AND CONDITIONS

Jun 06, 2021

This Agreement between University -- Nayara Carral ("You") and The American Association for the Advancement of Science ("The American Association for the Advancement of Science") consists of your license details and the terms and conditions provided by The American Association for the Advancement of Science and Copyright Clearance Center.

License Number	5083170913019
License date	Jun 06, 2021
Licensed Content Publisher	The American Association for the Advancement of Science
Licensed Content Publication	Science
Licensed Content Title	Very Large Capacitance Enhancement in a Two- Dimensional Electron System
Licensed Content Author	Lu Li,C. Richter,S. Paetel,T. Kopp,J. Mannhart,R. C. Ashoori
Licensed Content Date	May 13, 2011
Licensed Content Volume	332
Licensed Content Issue	6031

Volume number	332
Issue number	6031
Type of Use	Thesis / Dissertation
Requestor type	Scientist/individual at a research institution
Format	Electronic
Portion	Text Excerpt
Number of pages requested	2
Title	Enhancement of negative compressibility in two-dimensional electron gases at oxide interfaces.
Institution name	University of Cantabria
Expected presentation date	Jul 2021
Portions	Figure 2, Figure 4
Requestor Location	University Santander
	Santander, 39005 Spain Attn: University
Total	0.00 EUR

Terms and Conditions

American Association for the Advancement of Science TERMS AND CONDITIONS

Regarding your request, we are pleased to grant you non-exclusive, non-transferable permission, to republish the AAAS material identified above in your work identified above, subject to the terms and conditions herein. We must be contacted for permission for any uses other than those specifically identified in your request above.

The following credit line must be printed along with the AAAS material: "From [Full Reference Citation]. Reprinted with permission from AAAS."

All required credit lines and notices must be visible any time a user accesses any part of the AAAS material and must appear on any printed copies and authorized user might make.

This permission does not apply to figures / photos / artwork or any other content or materials included in your work that are credited to non-AAAS sources. If the requested material is sourced to or references non-AAAS sources, you must obtain authorization from that source as well before using that material. You agree to hold harmless and indemnify AAAS against any claims arising from your use of any content in your work that is credited to non-AAAS sources.

If the AAAS material covered by this permission was published in Science during the years 1974 - 1994, you must also obtain permission from the author, who may grant or withhold permission, and who may or may not charge a fee if permission is granted. See original article for author's address. This condition does not apply to news articles.

The AAAS material may not be modified or altered except that figures and tables may be modified with permission from the author. Author permission for any such changes must be secured prior to your use.

Whenever possible, we ask that electronic uses of the AAAS material permitted herein include a hyperlink to the original work on AAAS's website (hyperlink may be embedded in the reference citation).

AAAS material reproduced in your work identified herein must not account for more than 30% of the total contents of that work.

AAAS must publish the full paper prior to use of any text.

AAAS material must not imply any endorsement by the American Association for the Advancement of Science.

This permission is not valid for the use of the AAAS and/or Science logos.

AAAS makes no representations or warranties as to the accuracy of any information contained in the AAAS material covered by this permission, including any warranties of

merchantability or fitness for a particular purpose.

If permission fees for this use are waived, please note that AAAS reserves the right to charge for reproduction of this material in the

future.

Permission is not valid unless payment is received within sixty (60) days of the issuance of this permission. If payment is not received within this time period then all rights granted herein shall be revoked and this permission will be considered null and void.

In the event of breach of any of the terms and conditions herein or any of CCC's Billing and Payment terms and conditions, all rights granted herein shall be revoked and this permission will be considered null and void.

AAAS reserves the right to terminate this permission and all rights granted herein at its discretion, for any purpose, at any time. In the event that AAAS elects to terminate this permission, you will have no further right to publish, publicly perform, publicly display, distribute or otherwise use any matter in which the AAAS content had been included, and all fees paid hereunder shall be fully refunded to you. Notification of termination will be sent to the contact information as supplied by you during the request process and termination shall be immediate upon sending the notice. Neither AAAS nor CCC shall be liable for any costs, expenses, or damages you may incur as a result of the termination of this permission, beyond the refund noted above.

This Permission may not be amended except by written document signed by both parties.

The terms above are applicable to all permissions granted for the use of AAAS material. Below you will find additional conditions that apply to your particular type of use.

FOR A THESIS OR DISSERTATION

If you are using figure(s)/table(s), permission is granted for use in print and electronic versions of your dissertation or thesis. A full text article may be used in print versions only of a dissertation or thesis.

Permission covers the distribution of your dissertation or thesis on demand by ProQuest / UMI, provided the AAAS material covered by this permission remains in situ.

If you are an Original Author on the AAAS article being reproduced, please refer to your License to Publish for rules on reproducing your paper in a dissertation or thesis.

FOR JOURNALS:

Permission covers both print and electronic versions of your journal article, however the AAAS material may not be used in any manner other than within the context of your article.

FOR BOOKS/TEXTBOOKS:

If this license is to reuse figures/tables, then permission is granted for non-exclusive world rights in all languages in both print and electronic formats (electronic formats are defined below).

If this license is to reuse a text excerpt or a full text article, then

permission is granted for non-exclusive world rights in English only. You have the option of securing either print or electronic rights or both, but electronic rights are not automatically granted and do garner additional fees. Permission for translations of text excerpts or full text articles into other languages must be obtained separately.

Licenses granted for use of AAAS material in electronic format books/textbooks are valid only in cases where the electronic version is equivalent to or substitutes for the print version of the book/textbook. The AAAS material reproduced as permitted herein must remain in situ and must not be exploited separately (for example, if permission covers the use of a full text article, the article may not be offered for access or for purchase as a stand-alone unit), except in the case of permitted textbook companions as noted below.

You must include the following notice in any electronic versions, either adjacent to the reprinted AAAS material or in the terms and conditions for use of your electronic products: "Readers may view, browse, and/or download material for temporary copying purposes only, provided these uses are for noncommercial personal purposes. Except as provided by law, this material may not be further reproduced, distributed, transmitted, modified, adapted, performed, displayed, published, or sold in whole or in part, without prior written permission from the publisher."

If your book is an academic textbook, permission covers the following companions to your textbook, provided such companions are distributed only in conjunction with your textbook at no additional cost to the user:

- Password-protected website
- Instructor's image CD/DVD and/or PowerPoint resource
- Student CD/DVD

All companions must contain instructions to users that the AAAS material may be used for non-commercial, classroom purposes only. Any other uses require the prior written permission from AAAS.

If your license is for the use of AAAS Figures/Tables, then the electronic rights granted herein permit use of the Licensed Material in any Custom Databases that you distribute the electronic versions of your textbook through, so long as the Licensed Material remains within the context of a chapter of the title identified in your request and cannot be downloaded by a user as an independent image file.

Rights also extend to copies/files of your Work (as described above) that you are required to provide for use by the visually and/or print disabled in compliance with state and federal laws.

This permission only covers a single edition of your work as identified in your request.

FOR NEWSLETTERS:

Permission covers print and/or electronic versions, provided the AAAS material reproduced as permitted herein remains in situ and is not

exploited separately (for example, if permission covers the use of a full text article, the article may not be offered for access or for purchase as a stand-alone unit)

FOR ANNUAL REPORTS:

Permission covers print and electronic versions provided the AAAS material reproduced as permitted herein remains in situ and is not exploited separately (for example, if permission covers the use of a full text article, the article may not be offered for access or for purchase as a stand-alone unit)

FOR PROMOTIONAL/MARKETING USES:

Permission covers the use of AAAS material in promotional or marketing pieces such as information packets, media kits, product slide kits, brochures, or flyers limited to a single print run. The AAAS Material may not be used in any manner which implies endorsement or promotion by the American Association for the Advancement of Science (AAAS) or Science of any product or service. AAAS does not permit the reproduction of its name, logo or text on promotional literature.

If permission to use a full text article is permitted, The Science article covered by this permission must not be altered in any way. No additional printing may be set onto an article copy other than the copyright credit line required above. Any alterations must be approved in advance and in writing by AAAS. This includes, but is not limited to, the placement of sponsorship identifiers, trademarks, logos, rubber stamping or self-adhesive stickers onto the article copies.

Additionally, article copies must be a freestanding part of any information package (i.e. media kit) into which they are inserted. They may not be physically attached to anything, such as an advertising insert, or have anything attached to them, such as a sample product. Article copies must be easily removable from any kits or informational packages in which they are used. The only exception is that article copies may be inserted into three-ring binders.

FOR CORPORATE INTERNAL USE:

The AAAS material covered by this permission may not be altered in any way. No additional printing may be set onto an article copy other than the required credit line. Any alterations must be approved in advance and in writing by AAAS. This includes, but is not limited to the placement of sponsorship identifiers, trademarks, logos, rubber stamping or self-adhesive stickers onto article copies.

If you are making article copies, copies are restricted to the number indicated in your request and must be distributed only to internal employees for internal use.

If you are using AAAS Material in Presentation Slides, the required credit line must be visible on the slide where the AAAS material will be reprinted

If you are using AAAS Material on a CD, DVD, Flash Drive, or the World Wide Web, you must include the following notice in any electronic

versions, either adjacent to the reprinted AAAS material or in the terms and conditions for use of your electronic products: "Readers may view, browse, and/or download material for temporary copying purposes only, provided these uses are for noncommercial personal purposes. Except as provided by law, this material may not be further reproduced, distributed, transmitted, modified, adapted, performed, displayed, published, or sold in whole or in part, without prior written permission from the publisher." Access to any such CD, DVD, Flash Drive or Web page must be restricted to your organization's employees only.

FOR CME COURSE and SCIENTIFIC SOCIETY MEETINGS:

Permission is restricted to the particular Course, Seminar, Conference, or Meeting indicated in your request. If this license covers a text excerpt or a Full Text Article, access to the reprinted AAAS material must be restricted to attendees of your event only (if you have been granted electronic rights for use of a full text article on your website, your website must be password protected, or access restricted so that only attendees can access the content on your site).

If you are using AAAS Material on a CD, DVD, Flash Drive, or the World Wide Web, you must include the following notice in any electronic versions, either adjacent to the reprinted AAAS material or in the terms and conditions for use of your electronic products: "Readers may view, browse, and/or download material for temporary copying purposes only, provided these uses are for noncommercial personal purposes. Except as provided by law, this material may not be further reproduced, distributed, transmitted, modified, adapted, performed, displayed, published, or sold in whole or in part, without prior written permission from the publisher."

FOR POLICY REPORTS:

These rights are granted only to non-profit organizations and/or government agencies. Permission covers print and electronic versions of a report, provided the required credit line appears in both versions and provided the AAAS material reproduced as permitted herein remains in situ and is not exploited separately.

FOR CLASSROOM PHOTOCOPIES:

Permission covers distribution in print copy format only. Article copies must be freestanding and not part of a course pack. They may not be physically attached to anything or have anything attached to them.

FOR COURSEPACKS OR COURSE WEBSITES:

These rights cover use of the AAAS material in one class at one institution. Permission is valid only for a single semester after which the AAAS material must be removed from the Electronic Course website, unless new permission is obtained for an additional semester. If the material is to be distributed online, access must be restricted to students and instructors enrolled in that particular course by some means of password or access control.

FOR WEBSITES:

You must include the following notice in any electronic versions, either adjacent to the reprinted AAAS material or in the terms and conditions

for use of your electronic products: "Readers may view, browse, and/or download material for temporary copying purposes only, provided these uses are for noncommercial personal purposes. Except as provided by law, this material may not be further reproduced, distributed, transmitted, modified, adapted, performed, displayed, published, or sold in whole or in part, without prior written permission from the publisher."

Permissions for the use of Full Text articles on third party websites are granted on a case by case basis and only in cases where access to the AAAS Material is restricted by some means of password or access control. Alternately, an E-Print may be purchased through our reprints department (brocheleau@rockwaterinc.com).

REGARDING FULL TEXT ARTICLE USE ON THE WORLD WIDE WEB IF YOU ARE AN 'ORIGINAL AUTHOR' OF A SCIENCE PAPER

If you chose "Original Author" as the Requestor Type, you are warranting that you are one of authors listed on the License Agreement as a "Licensed content author" or that you are acting on that author's behalf to use the Licensed content in a new work that one of the authors listed on the License Agreement as a "Licensed content author" has written.

Original Authors may post the 'Accepted Version' of their full text article on their personal or on their University website and not on any other website. The 'Accepted Version' is the version of the paper accepted for publication by AAAS including changes resulting from peer review but prior to AAAS's copy editing and production (in other words not the AAAS published version).

FOR MOVIES / FILM / TELEVISION:

Permission is granted to use, record, film, photograph, and/or tape the AAAS material in connection with your program/film and in any medium your program/film may be shown or heard, including but not limited to broadcast and cable television, radio, print, world wide web, and videocassette.

The required credit line should run in the program/film's end credits.

FOR MUSEUM EXHIBITIONS:

Permission is granted to use the AAAS material as part of a single exhibition for the duration of that exhibit. Permission for use of the material in promotional materials for the exhibit must be cleared separately with AAAS (please contact us at permissions@aaas.org).

FOR TRANSLATIONS:

Translation rights apply only to the language identified in your request summary above.

The following disclaimer must appear with your translation, on the first page of the article, after the credit line: "This translation is not an official translation by AAAS staff, nor is it endorsed by AAAS as accurate. In crucial matters, please refer to the official English-language version originally published by AAAS."

FOR USE ON A COVER:

Permission is granted to use the AAAS material on the cover of a journal issue, newsletter issue, book, textbook, or annual report in print and electronic formats provided the AAAS material reproduced as permitted herein remains in situ and is not exploited separately

By using the AAAS Material identified in your request, you agree to abide by all the terms and conditions herein.

Questions about these terms can be directed to the AAAS Permissions department permissions@aaas.org.

Other Terms and Conditions:

v 2

Questions? customercare@copyright.com or +1-855-239-3415 (toll free in the US) or +1-978-646-2777.

THE AMERICAN ASSOCIATION FOR THE ADVANCEMENT OF
SCIENCE LICENSE
TERMS AND CONDITIONS

Jun 06, 2021

This Agreement between University -- Nayara Carral ("You") and The American Association for the Advancement of Science ("The American Association for the Advancement of Science") consists of your license details and the terms and conditions provided by The American Association for the Advancement of Science and Copyright Clearance Center.

License Number	5083171414422
License date	Jun 06, 2021
Licensed Content Publisher	The American Association for the Advancement of Science
Licensed Content Publication	Science
Licensed Content Title	Oxide Interfaces—An Opportunity for Electronics
Licensed Content Author	J. Mannhart,D. G. Schlom
Licensed Content Date	Mar 26, 2010
Licensed Content Volume	327
Licensed Content Issue	5973

Volume number	327
Issue number	5973
Type of Use	Thesis / Dissertation
Requestor type	Scientist/individual at a research institution
Format	Electronic
Portion	Text Excerpt
Number of pages requested	1
Title	Enhancement of negative compressibility in two-dimensional electron gases at oxide interfaces.
Institution name	University of Cantabria
Expected presentation date	Jul 2021
Portions	Figure 4
Requestor Location	University Santander
	Santander, 39005 Spain Attn: University
Total	0.00 USD

Terms and Conditions

American Association for the Advancement of Science TERMS AND CONDITIONS

Regarding your request, we are pleased to grant you non-exclusive, non-transferable permission, to republish the AAAS material identified above in your work identified above, subject to the terms and conditions herein. We must be contacted for permission for any uses other than those specifically identified in your request above.

The following credit line must be printed along with the AAAS material: "From [Full Reference Citation]. Reprinted with permission from AAAS."

All required credit lines and notices must be visible any time a user accesses any part of the AAAS material and must appear on any printed copies and authorized user might make.

This permission does not apply to figures / photos / artwork or any other content or materials included in your work that are credited to non-AAAS sources. If the requested material is sourced to or references non-AAAS sources, you must obtain authorization from that source as well before using that material. You agree to hold harmless and indemnify AAAS against any claims arising from your use of any content in your work that is credited to non-AAAS sources.

If the AAAS material covered by this permission was published in Science during the years 1974 - 1994, you must also obtain permission from the author, who may grant or withhold permission, and who may or may not charge a fee if permission is granted. See original article for author's address. This condition does not apply to news articles.

The AAAS material may not be modified or altered except that figures and tables may be modified with permission from the author. Author permission for any such changes must be secured prior to your use.

Whenever possible, we ask that electronic uses of the AAAS material permitted herein include a hyperlink to the original work on AAAS's website (hyperlink may be embedded in the reference citation).

AAAS material reproduced in your work identified herein must not account for more than 30% of the total contents of that work.

AAAS must publish the full paper prior to use of any text.

AAAS material must not imply any endorsement by the American Association for the Advancement of Science.

This permission is not valid for the use of the AAAS and/or Science logos.

AAAS makes no representations or warranties as to the accuracy of any information contained in the AAAS material covered by this permission, including any warranties of

merchantability or fitness for a particular purpose.

If permission fees for this use are waived, please note that AAAS reserves the right to charge for reproduction of this material in the

future.

Permission is not valid unless payment is received within sixty (60) days of the issuance of this permission. If payment is not received within this time period then all rights granted herein shall be revoked and this permission will be considered null and void.

In the event of breach of any of the terms and conditions herein or any of CCC's Billing and Payment terms and conditions, all rights granted herein shall be revoked and this permission will be considered null and void.

AAAS reserves the right to terminate this permission and all rights granted herein at its discretion, for any purpose, at any time. In the event that AAAS elects to terminate this permission, you will have no further right to publish, publicly perform, publicly display, distribute or otherwise use any matter in which the AAAS content had been included, and all fees paid hereunder shall be fully refunded to you. Notification of termination will be sent to the contact information as supplied by you during the request process and termination shall be immediate upon sending the notice. Neither AAAS nor CCC shall be liable for any costs, expenses, or damages you may incur as a result of the termination of this permission, beyond the refund noted above.

This Permission may not be amended except by written document signed by both parties.

The terms above are applicable to all permissions granted for the use of AAAS material. Below you will find additional conditions that apply to your particular type of use.

FOR A THESIS OR DISSERTATION

If you are using figure(s)/table(s), permission is granted for use in print and electronic versions of your dissertation or thesis. A full text article may be used in print versions only of a dissertation or thesis.

Permission covers the distribution of your dissertation or thesis on demand by ProQuest / UMI, provided the AAAS material covered by this permission remains in situ.

If you are an Original Author on the AAAS article being reproduced, please refer to your License to Publish for rules on reproducing your paper in a dissertation or thesis.

FOR JOURNALS:

Permission covers both print and electronic versions of your journal article, however the AAAS material may not be used in any manner other than within the context of your article.

FOR BOOKS/TEXTBOOKS:

If this license is to reuse figures/tables, then permission is granted for non-exclusive world rights in all languages in both print and electronic formats (electronic formats are defined below).

If this license is to reuse a text excerpt or a full text article, then

permission is granted for non-exclusive world rights in English only. You have the option of securing either print or electronic rights or both, but electronic rights are not automatically granted and do garner additional fees. Permission for translations of text excerpts or full text articles into other languages must be obtained separately.

Licenses granted for use of AAAS material in electronic format books/textbooks are valid only in cases where the electronic version is equivalent to or substitutes for the print version of the book/textbook. The AAAS material reproduced as permitted herein must remain in situ and must not be exploited separately (for example, if permission covers the use of a full text article, the article may not be offered for access or for purchase as a stand-alone unit), except in the case of permitted textbook companions as noted below.

You must include the following notice in any electronic versions, either adjacent to the reprinted AAAS material or in the terms and conditions for use of your electronic products: "Readers may view, browse, and/or download material for temporary copying purposes only, provided these uses are for noncommercial personal purposes. Except as provided by law, this material may not be further reproduced, distributed, transmitted, modified, adapted, performed, displayed, published, or sold in whole or in part, without prior written permission from the publisher."

If your book is an academic textbook, permission covers the following companions to your textbook, provided such companions are distributed only in conjunction with your textbook at no additional cost to the user:

- Password-protected website
- Instructor's image CD/DVD and/or PowerPoint resource
- Student CD/DVD

All companions must contain instructions to users that the AAAS material may be used for non-commercial, classroom purposes only. Any other uses require the prior written permission from AAAS.

If your license is for the use of AAAS Figures/Tables, then the electronic rights granted herein permit use of the Licensed Material in any Custom Databases that you distribute the electronic versions of your textbook through, so long as the Licensed Material remains within the context of a chapter of the title identified in your request and cannot be downloaded by a user as an independent image file.

Rights also extend to copies/files of your Work (as described above) that you are required to provide for use by the visually and/or print disabled in compliance with state and federal laws.

This permission only covers a single edition of your work as identified in your request.

FOR NEWSLETTERS:

Permission covers print and/or electronic versions, provided the AAAS material reproduced as permitted herein remains in situ and is not

exploited separately (for example, if permission covers the use of a full text article, the article may not be offered for access or for purchase as a stand-alone unit)

FOR ANNUAL REPORTS:

Permission covers print and electronic versions provided the AAAS material reproduced as permitted herein remains in situ and is not exploited separately (for example, if permission covers the use of a full text article, the article may not be offered for access or for purchase as a stand-alone unit)

FOR PROMOTIONAL/MARKETING USES:

Permission covers the use of AAAS material in promotional or marketing pieces such as information packets, media kits, product slide kits, brochures, or flyers limited to a single print run. The AAAS Material may not be used in any manner which implies endorsement or promotion by the American Association for the Advancement of Science (AAAS) or Science of any product or service. AAAS does not permit the reproduction of its name, logo or text on promotional literature.

If permission to use a full text article is permitted, The Science article covered by this permission must not be altered in any way. No additional printing may be set onto an article copy other than the copyright credit line required above. Any alterations must be approved in advance and in writing by AAAS. This includes, but is not limited to, the placement of sponsorship identifiers, trademarks, logos, rubber stamping or self-adhesive stickers onto the article copies.

Additionally, article copies must be a freestanding part of any information package (i.e. media kit) into which they are inserted. They may not be physically attached to anything, such as an advertising insert, or have anything attached to them, such as a sample product. Article copies must be easily removable from any kits or informational packages in which they are used. The only exception is that article copies may be inserted into three-ring binders.

FOR CORPORATE INTERNAL USE:

The AAAS material covered by this permission may not be altered in any way. No additional printing may be set onto an article copy other than the required credit line. Any alterations must be approved in advance and in writing by AAAS. This includes, but is not limited to the placement of sponsorship identifiers, trademarks, logos, rubber stamping or self-adhesive stickers onto article copies.

If you are making article copies, copies are restricted to the number indicated in your request and must be distributed only to internal employees for internal use.

If you are using AAAS Material in Presentation Slides, the required credit line must be visible on the slide where the AAAS material will be reprinted

If you are using AAAS Material on a CD, DVD, Flash Drive, or the World Wide Web, you must include the following notice in any electronic

versions, either adjacent to the reprinted AAAS material or in the terms and conditions for use of your electronic products: "Readers may view, browse, and/or download material for temporary copying purposes only, provided these uses are for noncommercial personal purposes. Except as provided by law, this material may not be further reproduced, distributed, transmitted, modified, adapted, performed, displayed, published, or sold in whole or in part, without prior written permission from the publisher." Access to any such CD, DVD, Flash Drive or Web page must be restricted to your organization's employees only.

FOR CME COURSE and SCIENTIFIC SOCIETY MEETINGS:

Permission is restricted to the particular Course, Seminar, Conference, or Meeting indicated in your request. If this license covers a text excerpt or a Full Text Article, access to the reprinted AAAS material must be restricted to attendees of your event only (if you have been granted electronic rights for use of a full text article on your website, your website must be password protected, or access restricted so that only attendees can access the content on your site).

If you are using AAAS Material on a CD, DVD, Flash Drive, or the World Wide Web, you must include the following notice in any electronic versions, either adjacent to the reprinted AAAS material or in the terms and conditions for use of your electronic products: "Readers may view, browse, and/or download material for temporary copying purposes only, provided these uses are for noncommercial personal purposes. Except as provided by law, this material may not be further reproduced, distributed, transmitted, modified, adapted, performed, displayed, published, or sold in whole or in part, without prior written permission from the publisher."

FOR POLICY REPORTS:

These rights are granted only to non-profit organizations and/or government agencies. Permission covers print and electronic versions of a report, provided the required credit line appears in both versions and provided the AAAS material reproduced as permitted herein remains in situ and is not exploited separately.

FOR CLASSROOM PHOTOCOPIES:

Permission covers distribution in print copy format only. Article copies must be freestanding and not part of a course pack. They may not be physically attached to anything or have anything attached to them.

FOR COURSEPACKS OR COURSE WEBSITES:

These rights cover use of the AAAS material in one class at one institution. Permission is valid only for a single semester after which the AAAS material must be removed from the Electronic Course website, unless new permission is obtained for an additional semester. If the material is to be distributed online, access must be restricted to students and instructors enrolled in that particular course by some means of password or access control.

FOR WEBSITES:

You must include the following notice in any electronic versions, either adjacent to the reprinted AAAS material or in the terms and conditions

for use of your electronic products: "Readers may view, browse, and/or download material for temporary copying purposes only, provided these uses are for noncommercial personal purposes. Except as provided by law, this material may not be further reproduced, distributed, transmitted, modified, adapted, performed, displayed, published, or sold in whole or in part, without prior written permission from the publisher."

Permissions for the use of Full Text articles on third party websites are granted on a case by case basis and only in cases where access to the AAAS Material is restricted by some means of password or access control. Alternately, an E-Print may be purchased through our reprints department (brocheleau@rockwaterinc.com).

REGARDING FULL TEXT ARTICLE USE ON THE WORLD WIDE WEB IF YOU ARE AN 'ORIGINAL AUTHOR' OF A SCIENCE PAPER

If you chose "Original Author" as the Requestor Type, you are warranting that you are one of authors listed on the License Agreement as a "Licensed content author" or that you are acting on that author's behalf to use the Licensed content in a new work that one of the authors listed on the License Agreement as a "Licensed content author" has written.

Original Authors may post the 'Accepted Version' of their full text article on their personal or on their University website and not on any other website. The 'Accepted Version' is the version of the paper accepted for publication by AAAS including changes resulting from peer review but prior to AAAS's copy editing and production (in other words not the AAAS published version).

FOR MOVIES / FILM / TELEVISION:

Permission is granted to use, record, film, photograph, and/or tape the AAAS material in connection with your program/film and in any medium your program/film may be shown or heard, including but not limited to broadcast and cable television, radio, print, world wide web, and videocassette.

The required credit line should run in the program/film's end credits.

FOR MUSEUM EXHIBITIONS:

Permission is granted to use the AAAS material as part of a single exhibition for the duration of that exhibit. Permission for use of the material in promotional materials for the exhibit must be cleared separately with AAAS (please contact us at permissions@aaas.org).

FOR TRANSLATIONS:

Translation rights apply only to the language identified in your request summary above.

The following disclaimer must appear with your translation, on the first page of the article, after the credit line: "This translation is not an official translation by AAAS staff, nor is it endorsed by AAAS as accurate. In crucial matters, please refer to the official English-language version originally published by AAAS."

FOR USE ON A COVER:

Permission is granted to use the AAAS material on the cover of a journal issue, newsletter issue, book, textbook, or annual report in print and electronic formats provided the AAAS material reproduced as permitted herein remains in situ and is not exploited separately

By using the AAAS Material identified in your request, you agree to abide by all the terms and conditions herein.

Questions about these terms can be directed to the AAAS Permissions department permissions@aaas.org.

Other Terms and Conditions:

v 2

Questions? customercare@copyright.com or +1-855-239-3415 (toll free in the US) or +1-978-646-2777.



American Physical Society Reuse and Permissions License

23-Jun-2021

This license agreement between the American Physical Society ("APS") and Nayara Carral ("You") consists of your license details and the terms and conditions provided by the American Physical Society and SciPris.

Licensed Content Information

License Number: RNP/21/JUN/041491
License date: 23-Jun-2021
DOI: 10.1103/RevModPhys.84.1419
Title: Maximally localized Wannier functions: Theory and applications
Author: Nicola Marzari et al.
Publication: Reviews of Modern Physics
Publisher: American Physical Society
Cost: USD \$ 0.00

Request Details

Does your reuse require significant modifications: No
Specify intended distribution locations: Worldwide
Reuse Category: Reuse in a thesis/dissertation
Requestor Type: Student
Items for Reuse: Figures/Tables
Number of Figure/Tables: 1
Figure/Tables Details: Figure 1
Format for Reuse: Electronic

Information about New Publication:

University/Publisher: University of Cantabria
Title of dissertation/thesis: Enhancement of negative compressibility in two-dimensional electron gases at oxide interfaces.
Author(s): Nayara Carral Sainz
Expected completion date: Jul. 2021

License Requestor Information

Name: Nayara Carral
Affiliation: Individual
Email Id: nayara.carral@unican.es
Country: Spain

TERMS AND CONDITIONS

The American Physical Society (APS) is pleased to grant the Requestor of this license a non-exclusive, non-transferable permission, limited to Electronic format, provided all criteria outlined below are followed.

1. You must also obtain permission from at least one of the lead authors for each separate work, if you haven't done so already. The author's name and affiliation can be found on the first page of the published Article.
2. For electronic format permissions, Requestor agrees to provide a hyperlink from the reprinted APS material using the source material's DOI on the web page where the work appears. The hyperlink should use the standard DOI resolution URL, <http://dx.doi.org/{DOI}>. The hyperlink may be embedded in the copyright credit line.
3. For print format permissions, Requestor agrees to print the required copyright credit line on the first page where the material appears: "Reprinted (abstract/excerpt/figure) with permission from [(FULL REFERENCE CITATION) as follows: Author's Names, APS Journal Title, Volume Number, Page Number and Year of Publication.] Copyright (YEAR) by the American Physical Society."
4. Permission granted in this license is for a one-time use and does not include permission for any future editions, updates, databases, formats or other matters. Permission must be sought for any additional use.
5. Use of the material does not and must not imply any endorsement by APS.
6. APS does not imply, purport or intend to grant permission to reuse materials to which it does not hold copyright. It is the requestor's sole responsibility to ensure the licensed material is original to APS and does not contain the copyright of another entity, and that the copyright notice of the figure, photograph, cover or table does not indicate it was reprinted by APS with permission from another source.
7. The permission granted herein is personal to the Requestor for the use specified and is not transferable or assignable without express written permission of APS. This license may not be amended except in writing by APS.
8. You may not alter, edit or modify the material in any manner.
9. You may translate the materials only when translation rights have been granted.
10. APS is not responsible for any errors or omissions due to translation.
11. You may not use the material for promotional, sales, advertising or marketing purposes.
12. The foregoing license shall not take effect unless and until APS or its agent, Aptara, receives payment in full in accordance with Aptara Billing and Payment Terms and Conditions, which are incorporated herein by reference.
13. Should the terms of this license be violated at any time, APS or Aptara may revoke the license with no refund to you and seek relief to the fullest extent of the laws of the USA. Official written notice will be made using the contact information provided with the permission request. Failure to receive such notice will not nullify revocation of the permission.
14. APS reserves all rights not specifically granted herein.
15. This document, including the Aptara Billing and Payment Terms and Conditions, shall be the entire agreement between the parties relating to the subject matter hereof.